ANISOTROPY AND AGGREGATION IN SELF-ASSEMBLED POLYMER NANOCOMPOSITES

Benjamin J. Lindsay

A DISSERTATION

in

Chemical and Biomolecular Engineering

Presented to the Faculties of the University of Pennsylvania

in

Partial Fulfillment of the Requirements for the

Degree of Doctor of Philosophy

2019

Supervisor of Dissertation

Robert A. Riggleman
Associate Professor of Chemical and Biomolecular Engineering

Co-Supervisor of Dissertation

Russell J. Composto
Professor of Materials Science and Engineering

Graduate Group Chairperson

John C. Crocker, Professor of Chemical and Biomolecular Engineering

Dissertation Committee

Ravi Radhakrishnan, Professor of Bioengineering

Jeffrey Meth, Technical Fellow at DuPont

ANISOTROPY AND AGGREGATION IN SELF-ASSEMBLED POLYMER NANOCOMPOSITES

ACKNOWLEDGEMENT

Throughout my PhD, I have benefitted from a tremendous amount of support from many people. There is no way I could have done this alone, and I have many people to thank. First, I need to thank my advisors. Rob, you have been exactly the kind of mentor I was hoping for coming into my PhD. You have made yourself available whenever I needed help, and provided encouragement and criticism when I needed it. You gave me much needed flexibility and patience with my life situations of having a kid and moving across the country before my time was up. You were a pleasure to work with, and I wish everyone had the opportunity to work with an advisor like you. Russ, you were also a fantastic advisor from the experimental side even though I spent less time in your building. You were patient and helpful, and group meetings with you were really enlightening. Thank you as well for all the help and encouragement you gave me.

Next, the remaining committee members, Jeff and Ravi. Jeff, it was always a pleasure meeting with you early in my PhD. I could always see your passion for nanocomposites, and your ability to make connections between seemingly disconnected fields was very inspiring. I wish DuPont would not have cut that research project, but it was a pleasure while it lasted. Ravi, while I had fewer interactions with you, I am grateful for your help and advice at my proposal and (preemptively) for your feedback regarding my dissertation and dissertation defense. I've heard nothing but good things about you, and it's good to know that kind and caring advisors are providing good support for all the students they encounter.

My PhD experience was made so much better by the help an support from lab members and collaborators. Amit, in the short time that we overlapped, you provided a lot of career advice that led me in the right direction to a job that I'm very excited about. In addition, just by landing a great job yourself, you made it easier for me to see myself getting into a similar career. Also the desk that you left for me to steal was very nice. Thanks for that too. Jason, sitting next to you in that desk was a fun and interesting period of my life. You

brought much needed humor to the world of computational polymer nanocomposites. You also have the great quality of being able to take complicated concepts and explain them in ways that are understandable even for a new PhD student. Huikuan, for a while you were basically my 3rd advisor. You somehow managed to know something about almost every single question I asked you. I'm still amazed by the wealth of knowledge sitting in your brain, and I benefitted tremendously by sitting in the same room as you. Ziyu, you were always a great resource to bounce ideas off of and get a new perspective. I'm glad you joined our group, and it was a pleasure sharing the office in Towne with you while it lasted. Emily, you were a great source of knowledge on a lot of topics, and you brought a lot of humor into the lab, which I very much appreciated. Robert, you brought a lot of technical and scientific expertise to the lab. Discussing new ideas (research and otherwise) with you was always either helpful and insightful, or distracting and pointless in the best ways. Chris, your technical expertise was inspiring. Technical or scientific discussions with you always helped me learn more. As proof of that, I am currently writing this dissertation in VSCode because you introduced me to it. I am excited about the LAMMPS package you are building, and only wish I had the tenacity and collaborative mindset that you are exhibiting to follow through on that idea years ago. Nadia, it was always a pleasure working with you. Your professionalism and productivity were very impressive, and you were always able to communicate your findings and ideas very effectively so that even theory people like me could understand them. Boris, the library of information from journal articles embedded in your brain was always impressive and helpful. I'm still not sure how you fit all that in there, but I hope you keep it up. Francisco, your leadership, collaborative mindset, and scientific knowledge were inspiring. You were a kind, patient, and effective collaborator, and Arkema is lucky to have you as a scientist.

ABSTRACT

ANISOTROPY AND AGGREGATION IN SELF-ASSEMBLED POLYMER NANOCOMPOSITES

Benjamin J. Lindsay

Robert A. Riggleman

Russell J. Composto

Polymer nanocomposites (PNC) are an exciting class of materials with a wide array of applications. Whether the desired application involves isotropic or anisotropic polymer and particle structures, controlling aggregation and/or anisotropy in PNCs remains crucial to engineering composites with desired properties. Many methods have been developed to address these challenges. Three methods of interest include 1) the inclusion of anisotropic particles in the PNC, 2) block copolymers used as anisotropic templates to pattern particles, and 3) particle surface chemistry modification to increase dispersion. Significant experimental progress has been made in all three of these methods, but deeper fundamental understanding in each of these domains is necessary to continue to improve experimental control over PNCs. Efficient simulation methods like Polymer Nanocomposite Field Theory (PNC-FT) and Theoretically Informed Langevin Dynamics (TILD) are a powerful way to gain these insights when used alongside experiments. With regards to anisotropic particles, PNC-FT was used to gain a better understanding of an experimentally observed phenomenon where gold nanorods (NRs) were observed bridging cylindrical domains in a diblock copolymer film. The simulations supported the idea that the observed orientations were indeed energetically favorable and not just kinetically trapped, and found ranges of NR length where bridging is expected to be most favorable. With regards to using block copolymers as anisotropic templates, in addition to the bridging nanorod study just described, PNC-FT was used to investigate the effect of diblock domain deformation on

particle-particle interactions when particles are confined within a diblock domain. It was found that for an A-B diblock copolymer nanocomposite, domain deformation can lead to stronger particle-particle attraction compared to interactions within a homopolymer melt, with attraction strength and separation distance tunable by properties like grafted chain length and density, particle size, and diblock A-B repulsion strength. Finally, with regards to surface chemistry modification to increase dispersion, TILD was used to better understand particle clustering behavior as a function of particle volume fraction and particle-polymer attraction strength. It was discovered that particle cluster size distribution and cluster structure change relatively slowly over the sharp phase boundaries present in phase diagrams.

TABLE OF CONTENTS

LIST OF ILLUSTRATIONS

CHAPTER 1 : Introduction

Polymer nanocomposites (PNCs), or polymer with nanoparticles dispersed inside them, are an exciting class of materials with a wide variety of applications. By virtue of the high surface area to volume ratio of the nanoparticles, small volume fractions of particles can lead to many kinds of improvements, such as in thermal [90], optical [34, 5], electrical [22], and mechanical [64] properties. For almost any desired property improvement, at least one of the following factors plays a key role: 1) polymer and/or particle anisotropy, and 2) the particle dispersion state.

Particle or polymer anisotropy is crucial for engineering materials with directional properties. For example, graphite particles were added to a polymer resin to synthesize a flexible film with good through-plane thermal conduction [90]. The high aspect ratio of the graphite plates were critical to allow heat to pass directly through the particles from one face of the film to the other. Another way to achieve directed properties is to use diblock copolymers as a template. Depending on the relative lengths of the dissimilar blocks of the diblock chain, the polymer melt can microphase separate into anisotropic formations like lamellar or cylindrical domains [61]. Several studies have demonstrated that lamellar templates can preferentially direct spherical or anisotropic particles to a particular domain of the diblock melt [79, 54, 16, 60, 51]. Other studies have shown that grain boundaries in lamellar diblock copolymer films can be used to preferentially direct fillers like homopolymer or nanoparticles to those defects [81, 49, 58].

The particle dispersion or aggregation state is also very important. For example, Moll et al. have shown that in an athermal system of polymer grafted particles in a homopolymer melt, particles arranged in a network impart greater mechanical strength than particles arranged in spherical or sheet-like clusters [64]. That same study and several others have explored how dramatically different aggregate structures can be achieved by manipulating simple parameters like the polymer graft length and the polymer graft surface density [53].

Efficient simulation methods are important for explaining and directing experimental research into the development of PNC materials. There are several complementary approaches to simulating polymer systems, including Self-Consistent Field Theory (SCFT) [61]. and Polymer Reference Interaction Site Model (PRISM) [77]. Nanoparticles can be incorporated into each of these methods. For example, PRISM has been used to explore how surface interactions between particles and polymer influence the particle dispersion state [31, 32, 27] Fixed particles have been added in SCFT using cavity functions to represent particles. This method is called Hybrid Particle Field Theory (HPFT) and was first introduced by Sides et al [79]. Our lab has extended HPFT in a method called Polymer Nanocomposite Field Theory (PNC-FT) in which particles can be treated as field-based to more efficiently compute density distributions of particles [47]. We have also developed a dynamic method called Theoretically Informed Langevin Dynamics (TILD), formerly known as Dynamic Mean Field Theory (DMFT) [10], an efficient mesoscale method which allows us to capture approximate dynamics. Particles can be incorporated into TILD by calculating forces from the same pair potentials used in PNC-FT.

My work has primarily made use of PNC-FT and TILD because of their flexibility and ability to calculate real-space particle and polymer properties. In this dissertation, I describe my efforts in 3 main directions related to anisotropy and aggregation within PNC materials: nanorods in cylindrical diblock domains in Chapter 3, nanospheres in diblock domains in Chapter 4, and nanoparticles with attractive particle-polymer interactions in Chapter 5. All of this work is aimed at providing insights to help experimentalists improve the design of specialty PNC materials.

CHAPTER 2 : Simulation and Analysis Methods

2.1. Polymer Nanocomposite Field Theory

2.1.1. Generalized Model

In Chapters 3 and 4, diblock copolymer nanocomposite systems were simulated using both the HPFT method and the PNC Field Theory (PNC-FT) method previously developed in the Riggleman lab [47, 10, 48]. The diblock copolymer chains are modeled as discrete Gaussian chains with $P = P_A + P_B$ segments, where the statistical segment sizes and monomer volumes of the two blocks are assumed to be identical. For systems with grafted NPs, the grafted chains have chain length N. The mass of the coarse grain segments of the polymer chains in the PNC-FT framework is distributed over a unit Gaussian, which regularizes the theory against ultraviolet divergences. In both the HPFT and PNC-FT approaches, NPs are introduced as cavity functions that can be carried through the particle-to-field transformation or left as explicit particles (HPFT). This field-based representation of particles allows us to calculate probability distributions of NPs using either the mean field assumption or complex Langevin schemes.

The discrete Gaussian polymer chain connectivity is modeled using the harmonic bonding potential

$$\beta U_{ideal} = \sum_{i}^{n_D} \sum_{j}^{P-1} \frac{3\left|\mathbf{r}_{i,j} - \mathbf{r}_{i,j+1}\right|^2}{2b^2} + \sum_{i}^{n_{GA}} \sum_{j}^{N-1} \frac{3\left|\mathbf{r}_{i,j} - \mathbf{r}_{i,j+1}\right|^2}{2b^2} \tag{2.1}$$

where n_D is the number of diblock chains, n_{GA} is the number of grafted chains, and b is the statistical size of a polymer segment. Density deviations away from the bulk density, ρ_0, are penalized using a Helfand compressibility potential [28], given by

$$\beta U_{ex} = \frac{\kappa}{2\rho_0} \int d\mathbf{r} \left[\hat{\rho}_+(\mathbf{r}) - \rho_0\right]^2 \tag{2.2}$$

where $\hat{\rho}_+ = \hat{\rho}_{DA} + \hat{\rho}_{DB} + \hat{\rho}_{GA} + \hat{\rho}_P + \hat{\rho}_S$ is the spatially varying total density and κ controls the magnitude of the density fluctuations. In the limit $\kappa \to \infty$, the strictly incompressible model is recovered. $\hat{\rho}_{DA}$, $\hat{\rho}_{DB}$, $\hat{\rho}_{GA}$, $\hat{\rho}_P$, and $\hat{\rho}_S$ are the microscopic densities of the A-block of the diblock chain, B-block of the diblock chain, grafted chains, NPs, and confining surface respectively. A and B components are assumed to interact through a purely repulsive, Flory-like contact potential given by

$$\beta U_2 = \frac{\chi}{\rho_0} \int d\mathbf{r} \hat{\rho}_A(\mathbf{r}) \hat{\rho}_B(\mathbf{r}) \tag{2.3}$$

where the Flory parameter χ quantifies the magnitude of incompatibility between A and B components and $\hat{\rho}_A$ and $\hat{\rho}_B$ are the spatially varying sums of all components given A and B chemistries, respectively. For simulations with bare NPs, the particles are assumed to be A-like, such that $\hat{\rho}_A = \hat{\rho}_{DA} + \hat{\rho}_P$. For simulations with grafted NPs, the particles are assumed to be neutral, so $\hat{\rho}_A = \hat{\rho}_{DA} + \hat{\rho}_{GA}$. In both cases, $\hat{\rho}_B = \hat{\rho}_{DB}$.

It is assumed that the mass of each polymer segment is described by a Gaussian distribution about its center, such that $\hat{\rho}_K(\mathbf{r})$, the microscopic density of polymer segment type K, is given by

$$\hat{\rho}_K(\mathbf{r}) = \int d\mathbf{r}' h(\mathbf{r} - \mathbf{r}') \hat{\rho}_{K,c}(\mathbf{r}') = (h * \hat{\rho}_{K,c})(\mathbf{r}) \tag{2.4}$$

where the last expression introduces a shorthand notation for a convolution integral, $\hat{\rho}_{K,c}(\mathbf{r})$ is the distribution of polymer segment centers given by

$$\hat{\rho}_{K,c}(\mathbf{r}) = \sum_i^{n_K} \sum_j^{N_K} \delta(\mathbf{r} - \mathbf{r}_{i,j}) \tag{2.5}$$

and $h(\mathbf{r})$ is the Gaussian smearing function given by

$$h(\mathbf{r}) = \left(\frac{1}{2\pi a^2} \right)^{3/2} e^{-|\mathbf{r}|^2/2a^2} \tag{2.6}$$

where a is the smearing length scale.

In Chapter 4, some NPs are treated as field-based, and some are explicitly fixed in one position. The field-based particle density $\hat{\rho}_{PF}(\mathbf{r})$ and explicit particle density $\hat{\rho}_{PE}(\mathbf{r})$ are both given by

$$\hat{\rho}_{PK}(\mathbf{r}) = (\Gamma * \hat{\rho}_{PK,c})(\mathbf{r}) \tag{2.7}$$

where $\hat{\rho}_{PK}$ represents either $\hat{\rho}_{PF}$ or $\hat{\rho}_{PE}$, $\Gamma(\mathbf{r} - \mathbf{r}')$ is a smearing function that defines the shape of the particle, and $\hat{\rho}_{PK,c}(\mathbf{r})$ is the NP center distribution given by

$$\hat{\rho}_{PK,c}(\mathbf{r}) = \sum_{i}^{n_{PK}} \delta(\mathbf{r} - \mathbf{r}_i). \tag{2.8}$$

For explicit particles, since the particle positions are fixed, $\hat{\rho}_{PE}$ is a constant function of $\mathbf{r}$ such that

$$\hat{\rho}_{PE}(\mathbf{r}) = \sum_{i}^{n_{PE}} \Gamma(\mathbf{r} - \mathbf{r}_i) \tag{2.9}$$

For spherical particles in Chapter 4, the particle smearing function is given by

$$\Gamma(\mathbf{r} - \mathbf{r}') = \frac{\rho_0}{2} \mathrm{erfc}\left(\frac{|\mathbf{r} - \mathbf{r}'| - R_P}{\xi}\right) \tag{2.10}$$

where R_P is the particle radius and ξ controls the length over which the density changes from ρ_0 to 0. For nanorods in Chapter 3, the particle smearing function is given by

$$\Gamma(\mathbf{r} - \mathbf{r}') = \frac{\rho_0}{4} \mathrm{erfc}\left(\frac{|\mathbf{u} \cdot (\mathbf{r} - \mathbf{r}')| - L_P/2}{\xi}\right) \mathrm{erfc}\left(\frac{|\mathbf{u} \times (\mathbf{r} - \mathbf{r}')| - R_P}{\xi}\right) \tag{2.11}$$

where L_P is the nanorod length, and $\mathbf{u}$ is a constant unit vector pointing in the direction of the long axis of the nanorod. In Chapter 3, a confining surface is also used, meaning $\hat{\rho}_S$

is nonzero and is given by

$$\hat{\rho}_S(\mathbf{r}) = \frac{\rho_0}{2}\mathrm{erfc}\left(\frac{\min(r_z, L_z - r_z) - T_S}{\xi_S}\right) \tag{2.12}$$

where r_z is the z-component of $\mathbf{r}$, L_z is the box size in the z-dimension, T_S is the thickness of the confining surface, and ξ_S is the length scale over which the surface drops from a density of ρ_0 to a density of 0.

By employing a standard Hubbard-Stratonovich particle-to-field transformation [18, 9], a partition function can be obtained of the form

$$\mathcal{Z} = z_1 \int \mathcal{D}\{w\} e^{\mathcal{H}[\{w\}]} \tag{2.13}$$

where z_1 is a numerical prefactor containing the thermal de Broglie wavelengths and normalization constants from the Gaussian functional integrals used to decouple the particle interactions, and $\mathcal{H}$ is the effective Hamiltonian given by

$$\begin{aligned}\mathcal{H}[\{w\}] = \frac{\rho_0}{2\kappa}\int d\mathbf{r}\ w_+(\mathbf{r})^2 - i\rho_0 \int d\mathbf{r}\ w_+(\mathbf{r}) + \frac{\rho_0}{\chi}\int d\mathbf{r}\left[w_{AB}^{(+)}(\mathbf{r})^2 + w_{AB}^{(-)}(\mathbf{r})^2\right] \\ - n_D \ln Q_D\left[\mu_A, \mu_B\right] - n_{PF}\ln Q_{PF}\left[\mu_{PF}\right] + \int d\mathbf{r}\left[\hat{\rho}_{PE}(\mathbf{r}) + \hat{\rho}_S(\mathbf{r})\right] w_P(\mathbf{r}) \\ - n_{GAE}\int d\mathbf{r}\sigma_{GAE}(\mathbf{r}) \ln q_{GA}(N, \mathbf{r}).\end{aligned} \tag{2.14}$$

Here, $\{w\}$ represents the set of chemical potential fields $w_{AB}^{(+)}(\mathbf{r})$, $w_{AB}^{(-)}(\mathbf{r})$, and $w_+(\mathbf{r})$; μ_A and μ_B are defined by $\mu_K = (h * w_K)(\mathbf{r})$ where

$$w_A = i\left(w_+ + w_{AB}^{(+)}\right) - w_{AB}^{(-)}, \tag{2.15}$$

$$w_B = i\left(w_+ + w_{AB}^{(+)}\right) + w_{AB}^{(-)}, \tag{2.16}$$

and w_P is equal to w_A for bare particles or iw_+ for grafted particles. Q_D and Q_{PF} are the partition functions for a single diblock chain and a single field-based NP, respectively. Q_D

is calculated from the chain propagator $q(j, \mathbf{r})$,

$$Q_D[\mu_A, \mu_B] = \frac{1}{V} \int d\mathbf{r}\ q(P, \mathbf{r}) \tag{2.17}$$

with the chain propagator constructed by iterating a Chapman-Kolmogorov equation

$$q(j+1, \mathbf{r}) = e^{-\mu_K(\mathbf{r})} \int d\mathbf{r}\ \Phi(\mathbf{r} - \mathbf{r}') q(j, \mathbf{r}) \tag{2.18}$$

where K is either A or B depending on the type of segment $j+1$, $\Phi(\mathbf{r}-\mathbf{r}')$ is the normalized bond transition probability, and the initial condition is given by

$$q(1, \mathbf{r}) = e^{-\mu_A(\mathbf{r})}. \tag{2.19}$$

Q_{PF} is given by

$$Q_{PF}[\mu_{PF}] = \frac{1}{V} \int d\mathbf{r}\ e^{-\mu_{PF}(\mathbf{r})} \tag{2.20}$$

where μ_{PF} is given by

$$\mu_{PF}(\mathbf{r}) = (\Gamma * w_P)(\mathbf{r}) - \frac{n_{GAF}}{n_{PF}} (\Gamma_\sigma * \ln q_{GA})(\mathbf{r}). \tag{2.21}$$

For bare particles, the last term can be ignored since the number of A chains grafted to the particles, n_{GAF}, is 0. $\Gamma_\sigma(\mathbf{r} - \mathbf{r}')$ represents the distribution of grafting sites surrounding a single NP center and is given by the Gaussian distribution function

$$\Gamma_\sigma(\mathbf{r} - \mathbf{r}') = \frac{1}{\sigma_0} \exp\left[-\left(\frac{|\mathbf{r} - \mathbf{r}'| - R_P - \xi}{\xi} \right)^2 \right] \tag{2.22}$$

where σ_0 is a normalization factor that enforces $\int d\mathbf{r}\ \Gamma_\sigma(\mathbf{r}) = 1$. This function confines the grafting sites to a homogeneous, thin shell with a thickness $\sim 2\xi$ and a distance $R_P + \xi$ away from the particle center. q_{GA} is the chain propagator for the grafted chains and has

the same form as Equation 2.18. In the last term of Equation 2.14, n_{GAE} is the number of A chains grafted onto the surface of explicit NPs and σ_{GAE} is the constant distribution of grafting sites on explicit NPs given by

$$\sigma_{GAE}(\mathbf{r}) = \sum_{i}^{n_{PE}} \Gamma_{\sigma}(\mathbf{r} - \mathbf{r}_i). \tag{2.23}$$

For systems with bare particles, this term can be ignored since both n_{GAE} and σ_{GAE} are 0. Diblock A and B center densities were calculated as follows:

$$\tilde{\rho}_{DA}(\mathbf{r}) = \frac{n_D}{VQ_D} \sum_{j=1}^{P_A} q(j, \mathbf{r}) e^{-\mu_A(\mathbf{r})} q^{\dagger}(P - j, \mathbf{r}) \tag{2.24}$$

$$\tilde{\rho}_{DB}(\mathbf{r}) = \frac{n_D}{VQ_D} \sum_{j=P_A+1}^{P} q(j, \mathbf{r}) e^{-\mu_B(\mathbf{r})} q^{\dagger}(P - j, \mathbf{r}) \tag{2.25}$$

where $q^{\dagger}$ is the inverse diblock propagator with the same form as Equation 2.18, but starting from the B end of the chain, and with an initial condition given by

$$q(1, \mathbf{r}) = e^{-\mu_B(\mathbf{r})}. \tag{2.26}$$

NP center densities were calculated using

$$\tilde{\rho}_{PF}(\mathbf{r}) = \frac{n_{PF}}{VQ_{PF}} e^{-\mu_{PF}(\mathbf{r})}. \tag{2.27}$$

Grafted chain center densities were calculated using

$$\tilde{\rho}_{GAE} = n_{GAE} \sum_{j=1}^{N} q_{GA}(j, \mathbf{r}) e^{-\mu_A(\mathbf{r})} q^{\dagger}_{GA}(N - j, \mathbf{r}) \tag{2.28}$$

where $q^{\dagger}_{GA}$ is the complementary propagator of the grafted chains, and also follows the same

form as Equation 2.18 but with an initial condition given by

$$q(1, \mathbf{r}) = \frac{\sigma_{GAE}(\mathbf{r})}{q_{GA}(N, \mathbf{r})} e^{-\mu_A(\mathbf{r})}. \tag{2.29}$$

The total density for polymer segments of type $X \in \{DA, DB, GA, GAE\}$ chains is given by

$$\breve{\rho}_X(\mathbf{r}) = (h * \tilde{\rho}_X)(\mathbf{r}). \tag{2.30}$$

Several figures in this work plot ϕ_{DA}, the local volume fraction of A-diblock segments. This is given by

$$\phi_{DA}(\mathbf{r}) = \frac{\breve{\rho}_{DA}(\mathbf{r})}{\rho_0}. \tag{2.31}$$

2.1.2. Numerical Methods

Complex Langevin

To sample thermal fluctuations, the complex Langevin (CL) method [18, 19, 65, 46] was used, which has been shown to be an efficient sampling technique for fluctuating polymer field theoretic models [47, 2, 72, 71, 88]. The field variables w_+, $w_{AB}^{(+)}$, and $w_{AB}^{(-)}$ are sampled while updating according to

$$\frac{\partial w_K(\mathbf{r})}{\partial t} = -\lambda_K \frac{\partial \mathcal{H}}{\partial w_K(\mathbf{r})} + \eta(\mathbf{r}, t), \tag{2.32}$$

where t is not a physical time, but a pseudo integration time, $w_K \in \{w_+, w_{AB}^{(+)}, w_{AB}^{(-)}\}$, λ_K is the step rate applied to w_K, and η is Gaussian white noise with the statistics

$$\langle \eta(\mathbf{r}, t) \rangle = 0, \tag{2.33}$$

$$\langle \eta(\mathbf{r}, t) \eta(\mathbf{r}', t') \rangle = 2\lambda \delta(t - t') \delta(\mathbf{r} - \mathbf{r}'). \tag{2.34}$$

The functional derivatives used in Equation 2.32 are given by:

$$\frac{\partial \mathcal{H}}{\partial w_+(\mathbf{r})} = \frac{\rho_0}{\kappa} w_+(\mathbf{r}) - i\rho_0 + i\breve{\rho}_+(\mathbf{r}) \tag{2.35}$$

$$\frac{\partial \mathcal{H}}{\partial w_{AB}^{(+)}(\mathbf{r})} = \frac{2\rho_0}{\chi} w_{AB}^{(+)}(\mathbf{r}) + i\left[\breve{\rho}_A(\mathbf{r}) + \breve{\rho}_{DB}(\mathbf{r})\right] \tag{2.36}$$

$$\frac{\partial \mathcal{H}}{\partial w_{AB}^{(-)}(\mathbf{r})} = \frac{2\rho_0}{\chi} w_{AB}^{(-)}(\mathbf{r}) + \breve{\rho}_{DB}(\mathbf{r}) - \breve{\rho}_A(\mathbf{r}) \tag{2.37}$$

where

$$\breve{\rho}_+ = \breve{\rho}_{DA} + \breve{\rho}_{DB} + \breve{\rho}_{GA} + \breve{\rho}_{PF} + \hat{\rho}_{PE} + \hat{\rho}_S \tag{2.38}$$

and $\breve{\rho}_A(\mathbf{r})$ depends on whether bare, A-like particles are used or grafted particles with neutral cores are used. For bare, A-like particles,

$$\breve{\rho}_A = \breve{\rho}_{DA} + \breve{\rho}_{PF} + \hat{\rho}_{PE}, \tag{2.39}$$

and for grafted particles with neutral cores,

$$\breve{\rho}_A = \breve{\rho}_{DA} + \breve{\rho}_{GA}. \tag{2.40}$$

Note that the $(\mathbf{r})$ was left off of all terms in the previous three equations to reduce clutter. A first-order splitting scheme [55] was used to evolve the fields according to Equation 2.32. For the CL results shown in Chapter 4, each simulation was run for 100,000 iterations after equilibration, sampling every 50 iterations, and averaged over 20 replicates. Step sizes were set to $\lambda_+ \Delta t = \lambda_{AB}^{(+)} \Delta t = 0.005$ and $\lambda_{AB}^{(-)} \Delta t = 0.0005$.

Mean-Field Approximation

Most PNC-FT simulations described in this thesis made use of the mean-field approximation, which finds the field configuration at the saddle point where

$$\frac{\partial \mathcal{H}}{\partial w_+(\mathbf{r})} = \frac{\partial \mathcal{H}}{\partial w_{AB}^{(+)}(\mathbf{r})} = \frac{\partial \mathcal{H}}{\partial w_{AB}^{(-)}(\mathbf{r})} = 0. \tag{2.41}$$

The configuration that solve this system of equations is found by updating the fields w_K according to Equation 2.32, but with the Gaussian noise term set to 0.

2.1.3. Potential of Mean Force Calculation

In Chapter 4, potential of mean force (PMF) curves were generated to describe the free energy as a function of particle separation distance. Two different types of PMF curves were generated, which will be referred to as constrained and unconstrained PMFs. Constrained PMFs describe the free energy of a system with two NPs under the idealized condition that the particles are fixed to a line along the center of a cylindrical or lamellar domain, like two beads on an infinitely tight string. Unconstrained PMFs, on the other hand, relax this constraint and account for particles not exactly on the center line. All PMFs were generated using 3D simulations.

Each constrained PMF was generated by running a series of HPFT simulations (i.e. $n_{PE} = 2$ and $n_{PF} = 0$) with two explicit NPs held fixed along the center-line of a cylindrical or lamellar diblock domain over a range of interparticle distances. Figure 1 a) shows a 3D representation of the simulation box used to calculate the free energy of a cylindrical system with bare 1.2 R_g diameter particles whose centers are separated by a distance of $\Delta r = 12.5\ R_g$. Here, and in the remainder of this work, R_g refers to the radius of gyration of the diblock chains, which are held constant to a constant discretization of $P = 60$ in all simulations. Figure 1 b) shows A-segment volume fraction in a 2D slice through the diagonal of the simulation box. In both cases, red and blue regions represent regions of high and

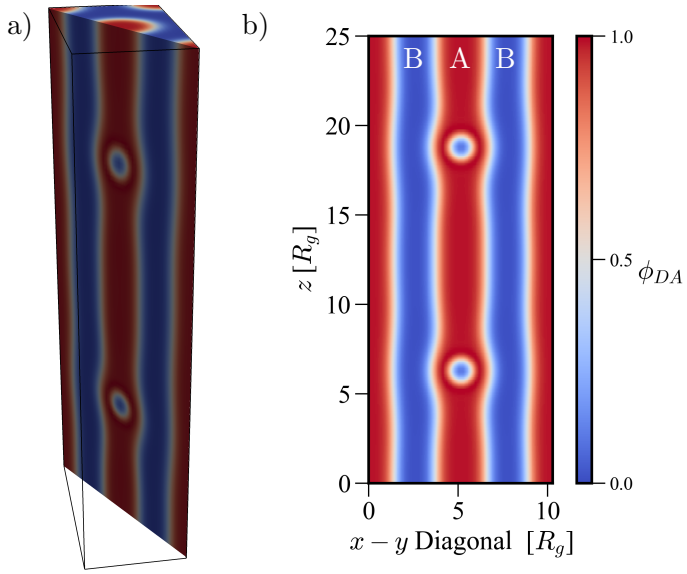

Figure 1: a) Constrained case showing 3D representation of A-segment density of cylindrical diblock simulation with 1.2 R_g diameter NPs. High and low A-segment densities shown in red and blue, respectively. b) A-segment density in 2D slice through diagonal of simulation box shown in a)

low A-segment density, respectively. The change in free energy (ΔF) from each simulation was computed using $\Delta F(\Delta r) = \mathcal{H}(\Delta r) - \mathcal{H}(\Delta r = \infty)$ where Δr is the interparticle center-to-center distance and $\mathcal{H}$ is the effective Hamiltonian of the system. In each case, ΔF is plotted against the interparticle surface-to-surface distance, $\Delta r - D_p$, where D_p is the NP diameter.

The unconstrained PMF was generated from a single SCFT simulation with one explicit NP and one field-based NP. Figure 2 a) shows a 3D representation of the simulation box used to generate the PMF for a cylindrical system with bare 1.2 R_g diameter particles. Figure 2 b) then shows the local number density of field-based NP centers in units of R_g^{-3}. The simulation method used here is the same as that used for the constrained PMFs, but with the added use of field-based NPs as has been previously described and implemented [47]. Additionally, selected PMFs were generated using fully-fluctuating field theoretic simulations in which thermal fluctuations were sampled using a complex Langevin implementation

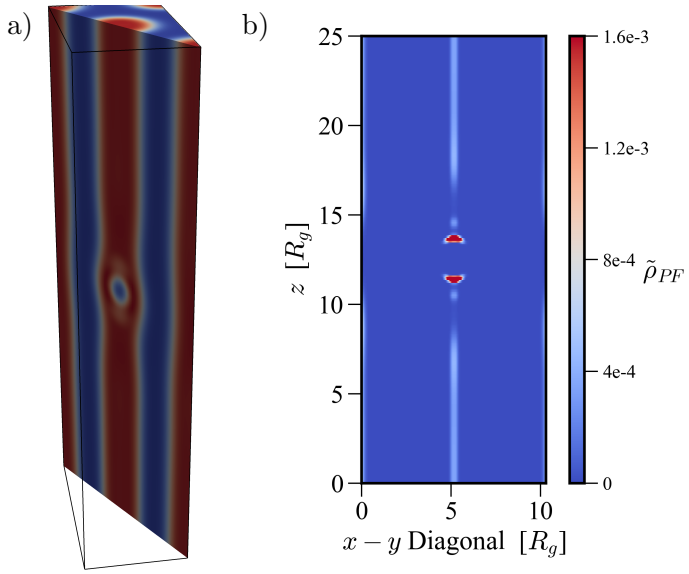

Figure 2: a) Unconstrained case showing a 3D representation of A-segment density of cylindrical diblock simulation with one particle fixed at z =12.5 R_g and one free 1.2 R_g diameter NP. High and low A-segment densities shown in red and blue, respectively. b) Number density of field-based NP centers in units of R_g^{-3} in 2D slice through diagonal of simulation box shown in a). This result shows that the most probable location of a second particle (red region) is adjacent to the fixed particle.

of the PNC-FT model [47]. The free energy was calculated using

$$\frac{\Delta F(\Delta r)}{k_B T} = -\ln\left(\frac{\rho_{PF,c,center}(\Delta r)}{\rho_{PF,c,center}(\Delta r=\infty)}\right), \tag{2.42}$$

where ρ_{FP} is the field-based NP center density along the center-line of the diblock domain in which the fixed particle resides. Density along the center-line is used to give a direct comparison with the constrained PMFs.

2.1.4. Box Size Optimization

Box size optimization was performed in Chapters 3 and 4 prior to production simulations by minimizing free energy per volume for bulk mean field systems with only field-based particles. In Chapter 3, the optimization was done with no nanoparticles in the system. In Chapter 4, the number of NPs was fixed at 2. This was done instead of holding the NP volume fraction fixed because exactly 2 NPs were required for constrained PMF generation.

For lamellar diblock systems, the box lengths in the y- and z-dimensions (L_y and L_z) were held fixed while the length in the x-dimension (L_x) was varied. For cylindrical diblock systems, a hexagonally close-packed (HCP) structure was enforced by fixing L_z and fixing $L_y/L_x = \sqrt{3}$ while varying L_x. In each case, the minimization was performed by running a series of independent simulations with varying box sizes and fitting a parabola to the free energy vs. box size to extract the minimum of the curve.

2.1.5. Potential Energy and Entropy Calculation

Constrained PMFs in Chapter 4 were analyzed to determine whether entropic or enthalpic effects dominated. Expressions for entropy and potential energy were derived using the thermodynamic relationships

$$U = T\left(\frac{\partial \log \mathcal{Z}}{\partial T}\right) \tag{2.43}$$

and

$$F = U - TS \tag{2.44}$$

under the mean field assumption and the assumption that both χ and κ are inversely related to temperature. Here and below, U, TS, and F are taken to be in units of k_BT. The expressions are

$$\Delta U = -\frac{\rho_0}{2\kappa}\int d\mathbf{r} w_+^2(\mathbf{r}) - \frac{\rho_0}{\chi}\int d\mathbf{r}\left(w_{AB}^{(+)^2}(\mathbf{r}) + w_{AB}^{(-)^2}(\mathbf{r})\right) \tag{2.45}$$

$$-T\Delta S = \Delta\mathcal{H} - \Delta U. \tag{2.46}$$

where the reference values for ΔU, $T\Delta S$, and $\Delta\mathcal{H}$ are all at $\Delta r = \infty$. A full derivation can be found in Appendix 7.1.

2.1.6. Nematic Order Parameter Calculation

In order to quantify alignment of polymer chains due to nearby particles in Chapter 4, nematic order parameter calculations were performed for several simulations. The derivation for this order parameter is an extension of the derivation presented by Prasad and coworkers [68], which is here adapted for a discrete Gaussian chain. The elements of the nematic order tensor S_{ij} (where $i, j \in \{x, y, z\}$) for the diblock are calculated as a function of position ($\mathbf{r}$), and are given by

$$S_{ij}(\mathbf{r}) = \frac{b^2}{36Q_d(N-1)} \sum_{s=1}^{N-1} \Bigg(q\nabla_i\nabla_j q^\dagger + q^\dagger\nabla_i\nabla_j q - \nabla_i q\nabla_j q^\dagger - \nabla_j q\nabla_i q^\dagger \\ - \frac{\delta_{ij}}{3}\left[q(\nabla\cdot\nabla)q^\dagger + q^\dagger(\nabla\cdot\nabla)q - 2(\nabla q)\cdot(\nabla q^\dagger)\right] \Bigg) \tag{2.47}$$

where q is a shorthand for $q(s, \mathbf{r})$ and $q^\dagger$ is a shorthand for $q^\dagger(N-s, \mathbf{r})$. The full derivation can be found in Appendix 7.2.

The diagonal elements $S_{ii}(\mathbf{r})$ can be interpreted as the strength of alignment of bond vectors in the i direction at position $\mathbf{r}$. Positive values indicate high bond stretching in the i direction, and negative values indicate compression in the i direction. The bond vectors are normalized by b, the expected bond length, but since our model employs Gaussian bonds, there is no strict maximum length and therefore no formal restriction of the nematic order parameter to the range $-1/2$ to 1.

To isolate diblock-specific effects on the polymer conformations, a residual nematic order parameter, S_{ij}^{res}, is used. This parameter is given by

$$S_{ij}^{res}(\mathbf{r}; \mathbf{r}_{P1}, \mathbf{r}_{P2}) = \ S_{ij}(\mathbf{r}; \mathbf{r}_{P1}, \mathbf{r}_{P2}) - S_{ij}^{h}(\mathbf{r}; \mathbf{r}_{P1}, \mathbf{r}_{P2}) \tag{2.48}$$

where S_{ij}^h is the nematic order for a simulation with A homopolymer instead of AB diblock, and $\mathbf{r}_{P1}$ and $\mathbf{r}_{P2}$ are the positions of the two fixed nanoparticles.

2.2. Theoretically Informed Langevin Dynamics

TILD allows efficient simulation of particles and polymers with approximate dynamics. A wide variety of particle types and polymer morphologies can be incorporated, but work in this thesis focused on bare nanoparticles with variable particle-polymer attraction.

2.2.1. Model

In Chapter 5, PNCs composed of homopolymer and spherical nanoparticles with a tunable attractive interaction to the homopolymer were simulated using TILD. The polymers are modeled as n_A discrete Gaussian chains with P segments each. The polymer microscopic center density is given by

$$\hat{\rho}_{A,c}(\mathbf{r}) = \sum_{i}^{n_A} \sum_{j}^{P} \delta(\mathbf{r} - \mathbf{r}_{i,j}) \tag{2.49}$$

and the smeared polymer density is given by

$$\hat{\rho}_{A}(\mathbf{r}) = (\hat{\rho}_{A,c} * h)(\mathbf{r}) \tag{2.50}$$

where $h(\mathbf{r})$ is a Gaussian smearing function given by Equation 2.6. The segments in the polymer chains are connected by a Gaussian bonding potential given by

$$\beta U_0 = \sum_{i}^{n_A} \sum_{j}^{P-1} \frac{3\left|\mathbf{r}_{i,j} - \mathbf{r}_{i,j+1}\right|^2}{2b^2} \tag{2.51}$$

To describe the particle-polymer interactions, a piecewise energy potential is introduced to allow mathematical control of an energy well near the surface of the particle. This function

is given by

$$u_{AP}(r) = \begin{cases} \kappa \text{ erfc}\left(\frac{|r-\sigma_P|}{\xi}\right) & r \leq \sigma_P \\ c_0 + c_1 r + c_2 r^2 + c_3 r^3 & \sigma_P < r < \sigma_P + \xi \\ 4\epsilon\left[\left(\frac{\sigma_{LJ}}{r-r_{\text{shift}}}\right)^{12} - \left(\frac{\sigma_{LJ}}{r-r_{\text{shift}}}\right)^{6}\right] & \sigma_P + \xi \leq r \end{cases} \tag{2.52}$$

This function is composed of 3 pieces: a volume exclusion repulsion for $r \leq \sigma_P$ similar to the spherical cavity functions that have been used in the past [47, 10, 48, 49, 50], a Lennard-Jones tail for $r \geq \sigma_P + \xi$, and a cubic spline connecting the two for $\sigma_P < r < \sigma_P + \xi$. In this function, κ controls the magnitude of the volume exclusion repulsion and σ_P controls the distance from the center at which the potential drops to $\kappa/2$. ϵ controls the depth of the energy well near the surface of the particle. ξ controls the distance over which the potential drops from κ to $\kappa/2$ as well as the distance from σ_P to the energy minimum. σ_{LJ} controls the length scale over which the tail end of the Lennard-Jones potential approaches 0. r_{shift} is a shift factor to fix the energy minimum of the potential at $r = \sigma_P + \xi$, and is given by

$$r_{\text{shift}} = \sigma_P + \xi - 2^{1/6}\sigma_{LJ}. \tag{2.53}$$

The middle piece of the piecewise function is a cubic spline to smoothly connect the repulsive and attractive pieces of the function. The parameters c_0, c_1, c_2, and c_3 are determined by solving this system of linear equations:

$$\begin{aligned} c_0 + c_1\sigma_P &+ c_2\sigma_P^2 &&+ c_3\sigma_P^3 &&= \kappa/2 \\ 0 + c_1 &&+ 2c_2\sigma_P &+ 3c_3\sigma_P^2 &&= \frac{\kappa}{\xi\sqrt{\pi}} \\ c_0 + c_1 R_m &+ c_2 R_m^2 &&+ c_3 R_m^3 &&= -\epsilon \\ 0 + c_1 &&+ 2c_2 R_m &+ 3c_3 R_m^2 &&= 0 \end{aligned}$$

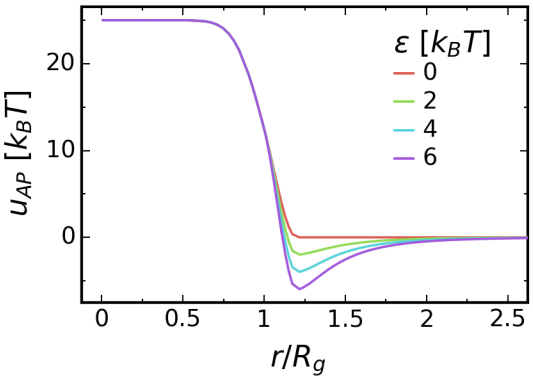

Figure 3: Particle-polymer pair potential curves for the range of ϵ values used in Chapter 5.

where $R_m = \sigma_P + \xi$, which represents the distance from the particle center to the energy minimum near the particle surface. Figure 3 shows u_{AP} curves for a few of the systems simulated in Chapter 5.

The particle center density is given by

$$\hat{\rho}_{P,c} = \sum_{i}^{n_P} \delta(\mathbf{r} - \mathbf{r}_i) \tag{2.54}$$

The smearing function for the nanoparticle, $\Gamma_P(\mathbf{r})$, is given by $u_{AP}(\mathbf{r}; \epsilon = 0)$, such that the function is nonnegative everywhere. With that definition, the microscopic particle density is given by

$$\hat{\rho}_P = (\hat{\rho}_{P,c} * \Gamma_P)(\mathbf{r}) \tag{2.55}$$

Total nonbonded interaction energies U_{AA}, U_{PP}, and U_{AP} can be generalized as

$$\beta U_{IJ} = \int d\mathbf{r} \int d\mathbf{r}' \hat{\rho}_{I,c}(\mathbf{r}) u_{IJ}(\mathbf{r} - \mathbf{r}') \hat{\rho}_{J,c}(\mathbf{r}') \tag{2.56}$$

where $u_{AA}(\mathbf{r}) = \frac{\kappa}{\rho_0}(h * h)(\mathbf{r})$, $u_{PP}(\mathbf{r}) = \frac{\kappa}{\rho_0}(\Gamma_P * \Gamma_P)(\mathbf{r})$, and u_{AP} is given by Equation 2.52.

Combining these, the total energy in the system is given by

$$\beta U = \beta U_0 + \beta U_{AA} + \beta U_{AP} + \beta U_{PP}. \tag{2.57}$$

2.2.2. Numerical Methods

TILD simulations are performed by iteratively updating polymer and particle positions according to an overdamped Langevin equation that ignores hydrodynamics for simplicity. The equation is written as

$$\frac{d\mathbf{r}_{k,s}}{dt} = D\beta \left[\mathbf{f}^b_{k,s}(t) + \mathbf{f}^{nb}_{k,s}(t)\right] + \mathbf{\Theta}_{k,s} \tag{2.58}$$

where $\mathbf{r}_{k,s}$ is the position of the sth monomer of the kth molecule, D is the monomeric diffusion coefficient, β is $1/k_BT$, $\mathbf{f}^b_{k,s}$ is the bonded force, $\mathbf{f}^{nb}_{k,s}$ is the nonbonded force, and $\mathbf{\Theta}_{k,s}$ is Gaussian white noise that satisfies

$$\langle \Theta_{k,s}(t) \rangle = 0 \tag{2.59}$$

$$\left\langle \Theta_{k,s}(t)\Theta_{k',s'}(t') \right\rangle = 2D\beta\delta_{k,k'}\delta_{s,s'}\delta_{t,t'}. \tag{2.60}$$

The bond potential in Equation 2.51 leads to a bond force of

$$\mathbf{f}^b_{k,s} = -\frac{3}{b^2}\left[(\mathbf{r}_{k,s} - \mathbf{r}_{k,s-1}) + (\mathbf{r}_{k,s} - \mathbf{r}_{k,s+1})\right] \tag{2.61}$$

where the first term is neglected for the first segment and the second term is neglected for the last segment of each chain. Note that the dependence on t has been removed for clarity in the previous equation. As has been shown previously [50, 11], nonbonded forces can be calculated efficiently from continuous density fields. In this case, $\tilde{\rho}_A(\mathbf{r}, t)$ and $\tilde{\rho}_P(\mathbf{r}, t)$ are the continuous density fields for monomer and nanoparticle centers, respectively, and are defined from the microscopic particle center densities using a first-order particle-to-mesh (PM) technique, which is a standard method for PM Ewald summations in particle-based

simulations of charged systems [29, 15, 20, 78]. The nonbonded force on polymer segment s of molecule k is given by

$$\mathbf{f}_{k,s}^{nb}(\mathbf{r},t) = -\int d\mathbf{r}'\nabla u_{AA}(\mathbf{r}-\mathbf{r}')\tilde{\rho}_A(\mathbf{r}'(t)) - \int d\mathbf{r}'\nabla u_{AP}(\mathbf{r}-\mathbf{r}')\tilde{\rho}_P(\mathbf{r}',t), \tag{2.62}$$

and similarly, the nonbonded force on nanoparticle k is given by

$$\mathbf{f}_{k}^{nb}(\mathbf{r},t) = -\int d\mathbf{r}'\nabla u_{AP}(\mathbf{r}-\mathbf{r}')\tilde{\rho}_A(\mathbf{r}'(t)) - \int d\mathbf{r}'\nabla u_{PP}(\mathbf{r}-\mathbf{r}')\tilde{\rho}_P(\mathbf{r}',t). \tag{2.63}$$

The Langevin equation was discretized using the method proposed by Grønbech-Jensen and Farago (GJF) [25], as was done in the work by Koski and coworkers [50].

2.2.3. Phase Diagram Calculation

In order to generate phase diagrams describing the macrophase separation or miscibility of nanoparticles, a method similar to that used by Koski et al. [50] was used. Simulation boxes with an aspect ratio ($AR = L_z/L_x = L_z/L_y$) of 4 or higher were initialized with nanoparticles in the center. Once the system reached equilibrium, average profiles of local particle volume fraction in the z-direction were computed such that

$$\phi_P(z) = \frac{\langle\rho_P(\mathbf{r})\rangle_{x,y}}{\langle\rho_A(\mathbf{r})\rangle_{x,y} + \langle\rho_P(\mathbf{r})\rangle_{x,y}}. \tag{2.64}$$

To extract the particle volume fractions in the particle-rich and particle-poor phases, the volume fraction curves were fitted with hyperbolic tangent curves of the form

$$\phi_{P,\text{fit}}(z) = \phi_{P,\text{poor}} + \frac{\phi_{P,\text{poor}} + \phi_{P,\text{rich}}}{2}\left(\tanh\left(\frac{w_f/2 - |L_z/2 - z|}{\xi_f}\right) + 1\right), \tag{2.65}$$

where $\phi_{P,\text{poor}}$, $\phi_{P,\text{rich}}$, w_f, and ξ_f are parameters to extract from the best fit curve, representing the particle volume fraction of the particle-poor phase, the particle volume fraction of the particle-rich phase, the width of the particle-rich phase, and the width of the in-

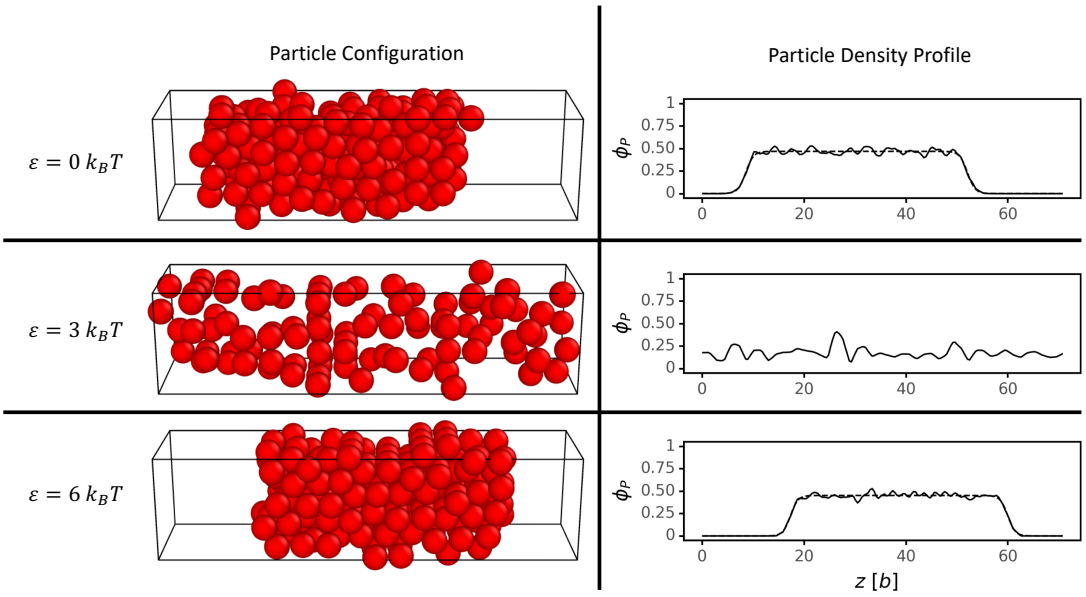

Figure 4: Representative particle configurations from long box simulations (left column) and corresponding particle volume fraction profiles (right column) for low to high ϵ values from top to bottom.

terface between the particle-poor and particle-rich phases. Figure 4 shows representative particle configurations and corresponding particle volume fraction profiles to demonstrate how volume points were generated for the phase diagram. These values were calculated for each equilibrated frame of the simulations, and the average values of $\phi_{P,\text{poor}}$, $\phi_{P,\text{rich}}$ from phase-separating simulations are plotted as pairs of points on a phase envelope with error bars representing standard deviation in phase diagrams in Chapter 5.

2.2.4. Cluster Analysis

Particle clusters were defined based on a contact cutoff distance, r_{cut}. A pair of particles was considered to be in contact if the Euclidean distance between them was less than r_{cut}. Unless otherwise specified, $r_{\text{cut}} = 1.125\ D_P$, where D_P is the particle diameter determined by the position of the first peak in g_{PP}, the particle-particle pair correlation function for particles of the same size with $\epsilon = 0$. Any two particles for which a path could be drawn from one to the other through particle contacts were considered part of the same cluster.

Within those clusters, a few different measurements were taken. The number of particles was counted in each cluster to determine cluster size distributions in different simulations. The coordination number of each particle was calculated, defined as the number of particles with which it was in contact.

CHAPTER 3 : Nanorods Bridging Diblock Copolymer Domains

3.1. Introduction

Nanoparticle (NP) position and orientation within polymer nanocomposites (PNCs) play critical roles in determining the resulting material properties. Block copolymers (BCPs) have been shown to be useful as templates for NP-BCP self-assembly to guide nanoparticles into desired positions and orientations [79, 54, 16, 60, 51]. This additional control may enable applications like the fabrication of integrated circuits using PNCs [80]. Thus, it is important to continue to improve our understanding of and control over NP-BCP self-assembly. NP-BCP self-assembly is typically guided by solvent annealing or thermal annealing a mixture of NPs and a BCP. BCPs can self-assemble into periodic, microphase-separated morphologies, enabling preferential localization of NPs into specific microphases, depending on the chemistry of the BCP microphases and the surface chemistry of the NPs.

Spherical NP-BCP self-assembly has been extensively studied [40, 13, 42, 43, 6, 57, 39, 94], but co-assembly of non-spherical NPs in BCPs is still an emerging area of research. [16, 85, 86, 84, 26, 66, 67, 69] In this work, the position and orientation of nanorods (NRs) in self-assembled BCPs with vertical domains were studied. The free energies of three different particle orientations as a function of NR length and diameter were studied with hybrid particle-field theory (HPFT) simulations, and orientations where the rod lies horizontally at the film surface were found to be the most energetically favorable. The simulations were in qualitative agreement with the experimental observation that the longer NRs prefer bridging over centered locations and that the shorter NRs prefer the centered locations. The simulations also reveal the existence of a wetting layer under NRs that bridge adjacent domains, but further from the NR, the cylindrical conformation remains unperturbed.

3.2. Methods

3.2.1. HPFT Model

Thin cylindrical diblock copolymer nanocomposite films were modeled with HPFT [79], which is a modified version of the PNC-FT model described in section 2.1.1. Only explicit particles were used, so $n_{PF} = 0$, and the NRs were bare, so $n_{GAE} = 0$. The simplified Hamiltonian is

$$\begin{aligned}\mathcal{H}[\{w\}] = \frac{\rho_0}{2\kappa}\int d\mathbf{r}\; w_+(\mathbf{r})^2 - i\rho_0\int d\mathbf{r}\; w_+(\mathbf{r}) + \frac{\rho_0}{\chi}\int d\mathbf{r}\left[w_{AB}^{(+)}(\mathbf{r})^2 + w_{AB}^{(-)}(\mathbf{r})^2\right] \\ - n_D \ln Q_D\left[\mu_A, \mu_B\right] + \int d\mathbf{r}\left[\hat{\rho}_{PE}(\mathbf{r}) + \hat{\rho}_S(\mathbf{r})\right] w_P(\mathbf{r})\end{aligned} \tag{3.1}$$

Neutral surfaces ($\hat{\rho}_S$) are included as cavity functions described in 2.12 to simulate the confinement seen in a thin film [10, 48]. The smearing length a used in equation 2.6 is 0.2 R_g where R_g is the ideal radius of gyration of the diblock copolymer

$$R_g = \sqrt{\frac{P-1}{6}}b. \tag{3.2}$$

To compute mean-field solutions, we evolve the fields according to

$$\left(\frac{\partial w_K(\mathbf{r})}{\partial t}\right) = -\lambda_K\left(\frac{\partial \mathcal{H}}{\partial w_K(\mathbf{r})}\right) \tag{3.3}$$

where λ_K is the relaxation coefficient for field w_K and t is a fictitious time. A first-order semi-implicit scheme [55] was used to numerically evolve the fields. For each free energy calculation, the vertical distance between the NR and the surface played a significant role in the resulting free energy since the interfaces are "soft", in that the surfaces of each are essentially a smoothed step function. In order to prevent this effect from dominating the free energy, the vertical position of the rod relative to the surface was chosen to minimize the free energy using Brent's method in each simulation [8].

3.2.2. System Dimensions

The experimental films upon which this work is based were prepared by spin-coating PS(M_n=180,000 g mol^{-1})-*b*-P2VP(M_n=77,000 g mol^{-1}) diblock from chloroform on silicon wafers, following the method of Yin et al [92]. The resulting films had a thickness of 363 nm, center-to-center distance between nearest neighbor cylinders (Δr_{ctc}) of 83 nm, and cylinder diameter of 43 nm. Two different NR lengths were used, 70 nm and 101 nm, which, importantly, were shorter and longer than Δr_{ctc}, respectively.

To model this system, a diblock Gaussian chain with $P_A = 18$ and $P_B = 42$ was used. χP was set to 30, which gives strong microphase separation, but is significantly lower than the expected χP for the experimental system. This choice was made because going to higher values of χP would significantly slow the simulations down. The size of one unit cell was determined using the box size optimization technique on neat diblock with no confinement, as discussed in section 2.1.4. For the neat BCP, the vertical cylinders had a Δr_{ctc} of 5.09 R_g and a diameter of 2.85 R_g. The thickness of the HPFT film was 9 R_g, which is sufficiently thick for the interface to not interact. Simulation boxes with two unit cells were used to provide enough space for NRs to fit when aligned horizontally. For comparison, in the experimental system, Δr_{ctc} was 6.03 $R_{g,\mathrm{exp}}$ the cylinder diameter was 3.12 $R_{g,\mathrm{exp}}$, and the film thickness was 26.36 $R_{g,\mathrm{exp}}$ where $R_{g,\mathrm{exp}}$ is the radius of gyration of PS(M_n=180,000 g mol^{-1})-*b*-P2VP(M_n=77,000 g mol^{-1}) Assuming Gaussian chain statistics with equal statistical segments sizes for both blocks, we calculate $R_{g,\mathrm{exp}}$=13.8 nm using b_{exp}=0.68 nm with a reference volume of 0.1 nm^3 [17]. The difference in parameters in the calculations and the experiments is likely due to the choice of χ. Higher χ leads to a larger domain spacing relative to the neat polymer R_g.

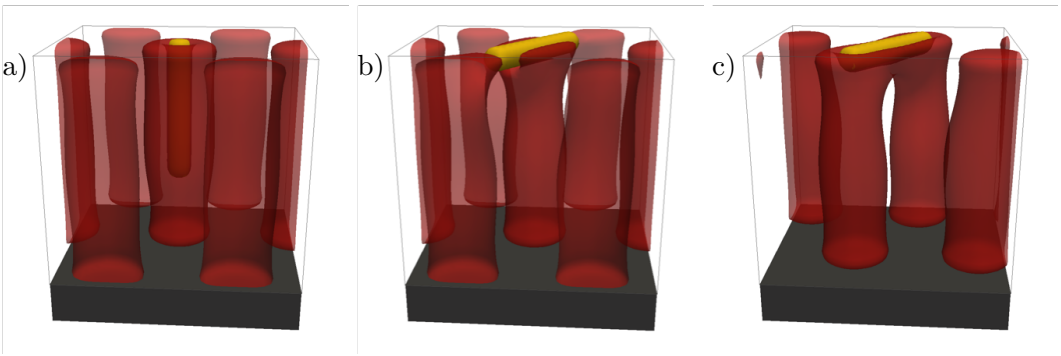

Figure 5: Representative cylindrical diblock configurations with a a) vertical, b) centered, and c) bridging NR at the surface.

3.3. Results and Discussion

3.3.1. Free Energy

In order to understand and predict likely positions and orientations of NRs near the surface of a HCP cylindrical diblock film, HPFT simulations were performed with NRs of different dimensions aligned in 3 different orientations which are referred to here as vertical, centered, and bridging, as shown in Figure 5. NRs with a vertical orientation were centered in a cylindrical A-domain with one end of the NR touching the surface. Centered and bridging rods were aligned horizontally at the surface of the film, with the particle either centered in a cylindrical A-domain or centered between two cylindrical A-domains such that the NR bridged the two domains if long enough. Centered rods were also aligned to point towards nearest neighbor cylindrical domains. These orientations were chosen based on commonly seen orientations in experiments.

In order to determine which configurations were most likely to be observed in experiments, NRs of different lengths and diameters were placed in each of the three orientations just described, and the free energy (ΔF) of the equilibrium configuration for each was recorded. HPFT is convenient for this purpose, because under the mean-field approximation, we have direct access to the free energy via the effective Hamiltonian. Since the experimental NRs are densely functionalized with short P2VP ligands, the simulations model the NR as though

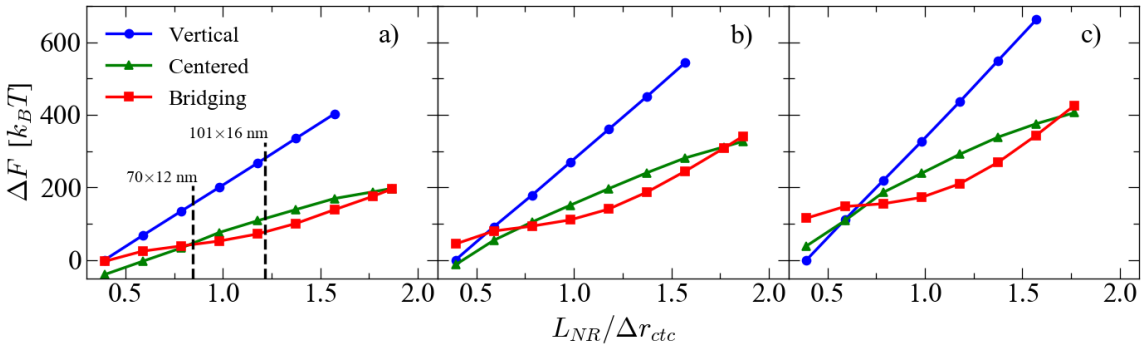

Figure 6: Mean-field free energy differences for NRs in different configurations as a function of NR length for NRs of diameter a) 1.0 R_g, b) 1.5 R_g, and c) 2.0 R_g. The NR length in the x-axis is normalized by the cylindrical domain nearest neighbor center-to-center distance, Δr_{ctc}. Free energy differences in each plot are calculated relative to the free energy of a rod of the same diameter and in the same configuration but with a length of 2 R_g, the shortest length in each case. The positions of the 101x16 nm and 70x12 nm rods used in experiments are marked in a) to show roughly where the experimental NR sizes fit into these calculations.

it has the same chemistry as the minority block of the copolymer, resulting in an athermal NR-monomer interaction with the cylinder-forming block.

Figure 6 shows the free energy calculations for all 3 NR diameters that were simulated, such that the plots in the figure correspond to NRs of different diameters 1.0, 1.5, and 2.0 R_g from left to right. Each plot has blue, green, and red points, corresponding to vertical, centered, or bridging NRs, respectively. Points of the same orientation are connected with lines as a guide to the eye. The x-axis corresponds to the NR length scaled by Δr_{ctc}, such that at a value of 1.0, a NR perfectly extends from the center of one cylindrical domain to the center of a nearest neighbor. The y-axis corresponds to the free energy of the system relative to the free energy of the system with the shortest vertical NR of the same diameter that was tested. This means that each of the 3 plots has a different reference free energy, but that within each plot, the points are comparable to each other. Note that the lowest vertical orientation point in each plot is 0.

The most prominent feature of the plots in figure 6 is that vertical rods of any appreciable length always have a higher ΔF compared to the horizontal rods. At the shortest NR length

simulated ($L_{NR} = 2R_g$), the bridging state and vertical state have similar free energies. This is because in the bridging state, the relative entropic favorability of increased contact between NR and the surface is balanced by the relative enthalpic penalty of increased contact between NR and PS. As $L_{NR}/\Delta r_{ctc}$ increases, the vertical state always has a greater free energy than the two horizontal states. The free energy increases more slowly for the horizontal states with the centered state being preferred up to $L_{NR}/\Delta r_{ctc} = 1.18$ and then transitioning to the bridging state with increasing $L_{NR}/\Delta r_{ctc}$.

The HPFT predictions can be compared with the two experimental systems. For the films with 101 nm NRs where $L_{NR}/\Delta r_{ctc} = 1.22$, Figure 6 a) shows that the bridging state (red) is thermodynamically favored, while the centered state is slightly less favorable and the vertical state is highly unfavorable. We can quantify the probability of finding a rod in a particular state S with

$$P(\mathrm{S}) = \frac{\exp(-\Delta F_{\mathrm{S}})}{\sum_{X\in\{B,C,V\}} \exp(-\Delta F_X)} \tag{3.4}$$

where B, C, and V represent the bridging, centered, and vertical states, respectively. At the 101 nm length, ($L_{NR}/r_{ctc,exp} = 1.22$) ΔF_B, ΔF_C, and ΔF_V are about 77.4, 114.3, and 280.6 k_BT, respectively. Equation 3.4 gives $P(B)$, $P(C)$, and $P(V)$ values of 1.0, 9.0×10^{-17}, and 5.5×10^{-89}, respectively, meaning that virtually all NRs should be in the bridging state, with negligible centered and vertical fractions. Comparing simulations with the experimental horizontal states, only the bridging state is observed for the 101 nm NRs, consistent with simulations. However, whereas the simulations predict that the vertical orientation is unfavorable, AFM and SEM scans from experiments show that some 101 nm NRS are found vertically oriented within the P2VP domain near the surface. Explanations for this discrepancy are given later. For films with 70 nm NRs where $L_{NR}/\Delta r_{ctc} = 0.84$, Figure 6 a) shows that the centered bridging state is slightly more favored than the bridging centered state and vertical is the least thermodynamically favored state. ΔF_B, ΔF_C, and ΔF_V are about 42.6, 45.6, and 153.7 k_BT, respectively, leading to probability estimates

of $P(B) = 0.95$, $P(C) = 0.05$, and $P(V) = 5.2 \times 10^{-49}$. This means the predicted ratio of bridging to centered rods is about 20:1, and the vertical state is again expected to be negligible. In experiments with 70 nm NRs, the bridging, the centered and vertical states are observed with the ratio of bridging to centered states being 3.5:1. The simulation results trend in a similar direction with the experiments in that the centered orientation is more preferable for the shorter NRs than for the longer ones. The experimental observation of centered NRs is consistent with the HPFT prediction, however, the results are not in quantitative agreement with the experiments.

There are several possible explanations for the quantitative differences between experiments and HPFT predictions. First, nanocomposite films were processed via solvent annealing where polymer and NRs co-assemble during swelling and solvent evaporation. As a result, NRs in the dry film may be kinetically trapped in thermodynamically unfavorable or metastable states. Due to the mean-field nature of the calculations, these kinetic effects are not represented in the simulations. Second, the simulations do not explicitly model the grafted polymers, and therefore these calculations would not capture any entropy associated with the grafted polymers that may be important. Finally, the experimental χP parameter is larger than those used in the simulations and we have assumed equal interactions (surface energy) of both blocks with the top surface.

3.3.2. Bridging Morphology

Visualizing the simulations leads to insights about the BCP morphology around bridging NRs that are difficult to access experimentally using SEM and AFM. Figure 7 shows the 3D field configuration and a 2D slice along the length of the NR, where the NR diameter and length are 1 Rg and 6 Rg, respectively, which approximates the dimensions of the 101 nm NR. Both representations show that blocks from the cylindrical domain (red) wet the underside of the bridging NR (gold) resulting in the two bridged vertical cylinders becoming connected into one arch shaped domain. The vertical cylinders forming each "column" of the arch remain intact. Note that the HPFT assumes symmetric wetting at the air/polymer and

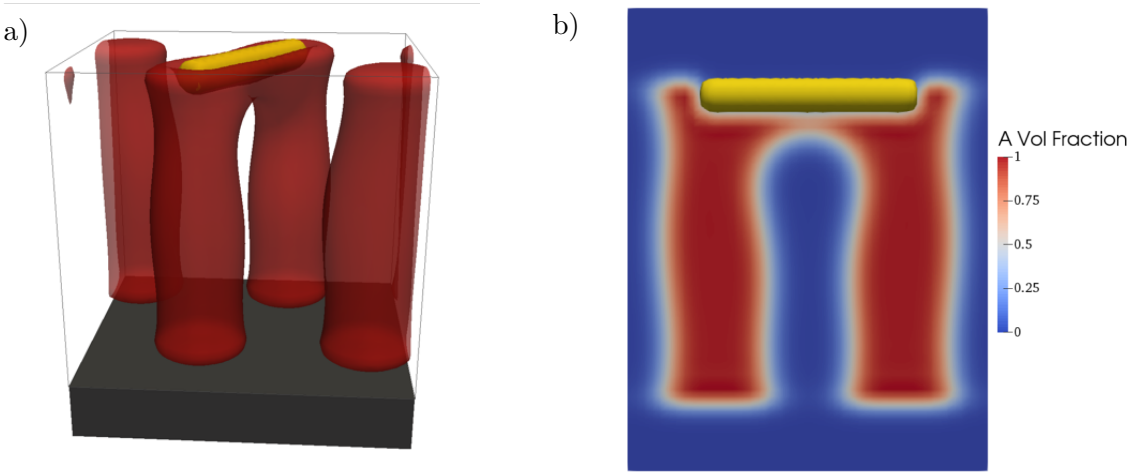

Figure 7: a) 3D visualization of the cylindrical domains of a simulation with NR diameter and length of 1 R_g and 6 R_g, respectively. Red surfaces and gold-colored surfaces represent isosurfaces at which the local A volume fraction and NR volume fraction, respectively, is 0.5. b) 2D density map of the diagonal plane taken along the length of the NR from a). Red and blue regions represent high and low, respectively, local A volume fraction, and the gold-colored surface matches the gold isosurface in a).

polymer/substrate interfaces. This suggests that in the experimental 101 nm NR system, a bridging NR induces a similar arch shape, connecting the two cylindrical domains.

3.4. Conclusions

This work supported experimental efforts to use NRs to bridge cylindrical BCP domains. Ranges of NR lengths where bridging is expected were found, which qualitatively agree with experiments. The expected morphology of BCP films beneath the surface of bridging NRs was discovered, which is difficult to access experimentally. This work, together with experimental efforts, provides a promising approach for developing new self-assembled BCP-NP devices.

CHAPTER 4 : Spherical Nanoparticle Interactions in Diblock Copolymer Domains

4.1. Introduction

Polymer nanocomposite (PNC) materials, or polymer melts with dispersed NPs, have become a topic of increasing interest due to unique combinations of properties they can exhibit. Compared to conventional filler materials, NPs have orders of magnitude higher surface area per volume, allowing them to induce significant changes in material properties even at low filler fractions [7]. PNCs have been shown to exhibit a wide variety of property enhancements, including mechanical [64], optical [34, 5], thermal [90], and electrical [22] properties, and control over NP dispersion is essential to achieving the desired effects. Significant research effort has gone into understanding the fundamental physics that will enable further advancements in PNC material properties for both homopolymer and diblock matrices [7, 30, 52]

The dispersion behavior of particles is relatively well understood in so-called "athermal" systems, where either the particle surface chemistry matches the polymer matrix chemistry, or polymer chains of the same chemistry as the matrix chains that have been grafted to the particles. Briefly, the dispersion depends primarily on P, the matrix degree of polymerization; N, the graft degree of polymerization; and σ, the graft density. When $P \ll N$, the system is in a "wet brush" regime where matrix chains and grafted chains are interdigitated, and when $P \gg N$, the system is in a "dry brush" regime where the entropic penalty for interdigitation is prohibitively high, and particles aggregate due to depletion—attraction forces [59, 70, 3, 62, 93, 1, 38, 44, 87, 12, 24, 33]. However, the interactions between NPs mediated by more complex matrices like block copolymer (BCP) melts have not been as rigorously studied.

BCP matrices enable microphase separated domains and are often used to control NP dispersion behavior [7, 76, 69]. This allows both enthalpic control (choice of graft chemistry) and entropic control (choice of graft length) over particle dispersion. The first BCP

nanocomposite syntheses were reported in the early 1990s [75]. Since then experimental studies have investigated the rich and complex thermodynamics in such systems, exploring, for example, the effect of particle size on position within BCP domains [82] and the NP loading at which macrophase separation occurs [91]. Work from Xu and coworkers has demonstrated that bottlebrush block copolymer matrices can guide NP self-assembly into a range of morphologies depending on volume fraction of grafted NPs [41]. Other work has explored the localization of NPs to block copolymer defects, demonstrating, for example, how defects in block copolymer domains can be used for directed self-assembly of nanocomposites with ordered NPs [45, 49] and how NP pinning at grain boundaries influences the grain coarsening of BCP nanocomposites [73, 74]. A few studies have demonstrated the ability to direct gold nanorods into diblock domains which could lead to materials with increased thermal or electrical conductivity along those domains [16, 56, 60, 69, 14]. A recent study showed that polymer grafted nanoplates can be directed into the favorable domain of a lamellar diblock copolymer [51]. A superassembly approach has also been used to create co-existing nanoplates and diblocks [35].

An alternative approach to achieve directed properties afforded by anisotropic particles like gold nanorods would be to disperse spherical NPs into the diblock domains in a way that they will self-assemble into long chain-like structures. However, even with spherical NPs, interactions between NPs and BCP matrices are not fully understood. One clear demonstration of the complex behavior of BCP nanocomposites was conducted by Lan and coworkers [54]. They dispersed PS-grafted silica NPs in a symmetric poly(styrene-*b*-butadiene) matrix and observed good dispersion with $P/N \lesssim 1$ in the dry-brush limit and aggregation with $P/N > 1$, exactly opposite of what is observed in athermal systems with a homopolymer matrix. Rationalizations were offered based on effective particle size compared to lamellar spacing as well as degree of solvation at the time of ordering, but a molecular view of this interpretation has remained elusive. Efficient simulation techniques can be a powerful complement to experiments to better understand particle interaction mechanisms at the molecular level.

These types of dense systems are expensive to simulate using particle-based approaches, whereas polymer field theory provides efficient pathways to explore BCP nanocomposites. Several theoretical studies have been performed based on polymer field theoretic simulations to elucidate the complex physics involved in BCP nanocomposites. Matsen et al. investigated the effect of a single NP on the nearby domain interfaces in a lamellar diblock matrix using self-consistent field theoretic (SCFT) simulations [63]. Other studies investigated the distribution of many particles. For example, several researchers have used SCFT with density functional theory (DFT) to predict particle distributions in diblock copolymer domains [83, 36, 37, 23]. Sides et al. developed a hybrid particle-field (HPF) method to predict particle dispersion while explicitly retaining particle location information [79]. Riggleman et al. have developed a framework called PNC field theory (PNC-FT) which generalizes the HPF treatment of NPs to efficiently allow fluctuations, grafted chains, and particle anisotropy in the simulations. Though these methods have been successfully used to study particle distributions, little is known about pairwise interactions between NPs in BCP domains.

Here, results are presented using PNC-FT simulations to systematically explore pairwise interactions between spherical NPs in diblock copolymer matrices. The results suggest that equilibrium particle spacing in diblock matrices can be finely controlled by tuning the particle diameter, the diblock to graft degree of polymerization ratio, and the graft density. They also show that attractive forces between particles can be much stronger in a diblock copolymer than in a homopolymer in some cases, and the effective interaction is mediated by both the entropy of the diblock matrix and the deformation of the A-B interface. This ability to tune the spacing between spherical NPs opens up pathways for anisotropic properties that would typically require more expensive anisotropic NPs such as gold nanorods. Grafted chains reduce particle-particle interaction strength, but when confined by domain interfaces, it is shown here that they can have a significantly reduced extension compared to what is expected for dewetted brush chains.

4.2. Numerical Methods and Parameters

Most results presented below were from simulations performed under the mean field (MF) approximation, but in some cases the complex Langevin (CL) method [18, 19, 65, 46], was used, which has been shown to efficiently sample fluctuations in polymer field theory [47, 2, 72, 71, 88]. The fields were evolved as was done previously [10] using a semi-implicit first-order splitting scheme [55]. In all calculations presented below, the diblock matrix chains are discretized into $P = 60$ segments, the matrix chain density parameter $C = \rho_0 R_g^3/P = 6$, and $\chi = 0.5$. For cylindrical systems, $P_A = 18$ and $P_B = 42$ were used, such that $f_A = 0.3$. For lamellar systems, $P_A = P_B = 30$ were used, such that $f_A = 0.5$. For bare NP systems, an incompressibility parameter of $\kappa = 6$ was used; NP diameters were set to 1.2 or 1.5 R_g; and the NP interfacial width parameter, ξ, and the polymer segment smearing length scale, a, were set to 0.2 R_g. For grafted NP systems, smaller NPs with a core diameter of 0.6 R_g were used. To avoid a sharp discontinuity at the center of the cavity function for these particles, ξ and a were decreased to 0.1 R_g. In order to successfully exclude polymer segments from these smaller particles, the incompressibility parameter was increased to $\kappa = 12$. Altering these parameters in the bare NP systems did not significantly change the resulting free energy differences. Grafted chains were discretized into either $N = 6$ or $N = 60$ segments, giving $P/N = 10$ and $P/N = 1$, respectively.

4.3. Results and Discussion

4.3.1. Bare Nanoparticles in Cylindrical and Lamellar Forming Copolymers

In order to isolate the role of matrix and grafted chains, diblock systems with bare NPs were studied using PNC-FT. Figure 8a) shows constrained PMFs for bare NPs of two different sizes ($D_P = 1.5$ R_g and 1.2 R_g) in the A domain of cylindrical and lamellar diblock copolymers. The PMF between two NPs in a homopolymer matrix is also shown for comparison. This system has the same input parameters as the cylindrical diblock system with $D_P = 1.5$ R_g, but with an A homopolymer of length $P = 60$ rather than

an A-B diblock with $P_A = 18$ and $P_B = 42$. These PMFs represent the free energy as a function of distance between the surfaces of two NPs, assuming the particles are axially constrained to the center of the cylindrical domain.

The PMFs have several common features that can be better understood by observing the diblock morphology associated with different points on the curves. The cylindrical domain contains two nanoparticles with diameters of 1.2 R_g and the PMF corresponding to the primary minimum (b), activated state (c) and secondary minimum (c) are denoted by solid circles in Figure 8a). Figures 8b)-d) show the A segment density in diagonal slices through cylindrical 1.2 R_g diameter particle at the first three extrema in 8a). At $\Delta r - D_P = 0$ (point b), corresponding to the two particles in contact, a primary minimum in free energy is observed. Note that the free energy is finite at and below 0 due to the soft walls of the NPs and weak compressibility in the HPF model. When the particle surfaces are separated by a distance of 1-2 R_g (point c), a local free energy maximum in the diblock is seen. The maxima for the lamellar conformations are significantly lower than for the cylindrical conformations. This reduced energy makes sense given that within a lamellar domain, a particle is confined by a smaller surface area of A-B interface compared to cylindrical domains, and suggests that forming particle aggregates should be easier in lamellar diblocks compared to cylindrical diblocks. Figure 8c) shows that at this point, the slight bulges induced by the particles in the A-B interface come together to form a region of high curvature in the interface between the particles. When the particle surfaces are separated by a distance of 4-5 R_g (point d), the bulges in the interface are sufficiently far apart to allow the high curvature associated with the maximum (Figure 8c) to relax. ΔF approaches 0 at higher particle separation. For the homopolymer (green line), the primary minimum is about a third of the cylindrical (solid black) and lamellar (dashed black) systems for $D_p = 1.5\ R_g$. The energy barrier is about an order of magnitude smaller, suggesting that the microphase-separated diblock copolymer matrix can significantly increase the strength of equilibrium particle-particle attraction. To the best of our knowledge, experimentalists have been unable to observe the bulge in the A-B interface depicted in 8b)-d), for reasons which are discussed later. However, the presence

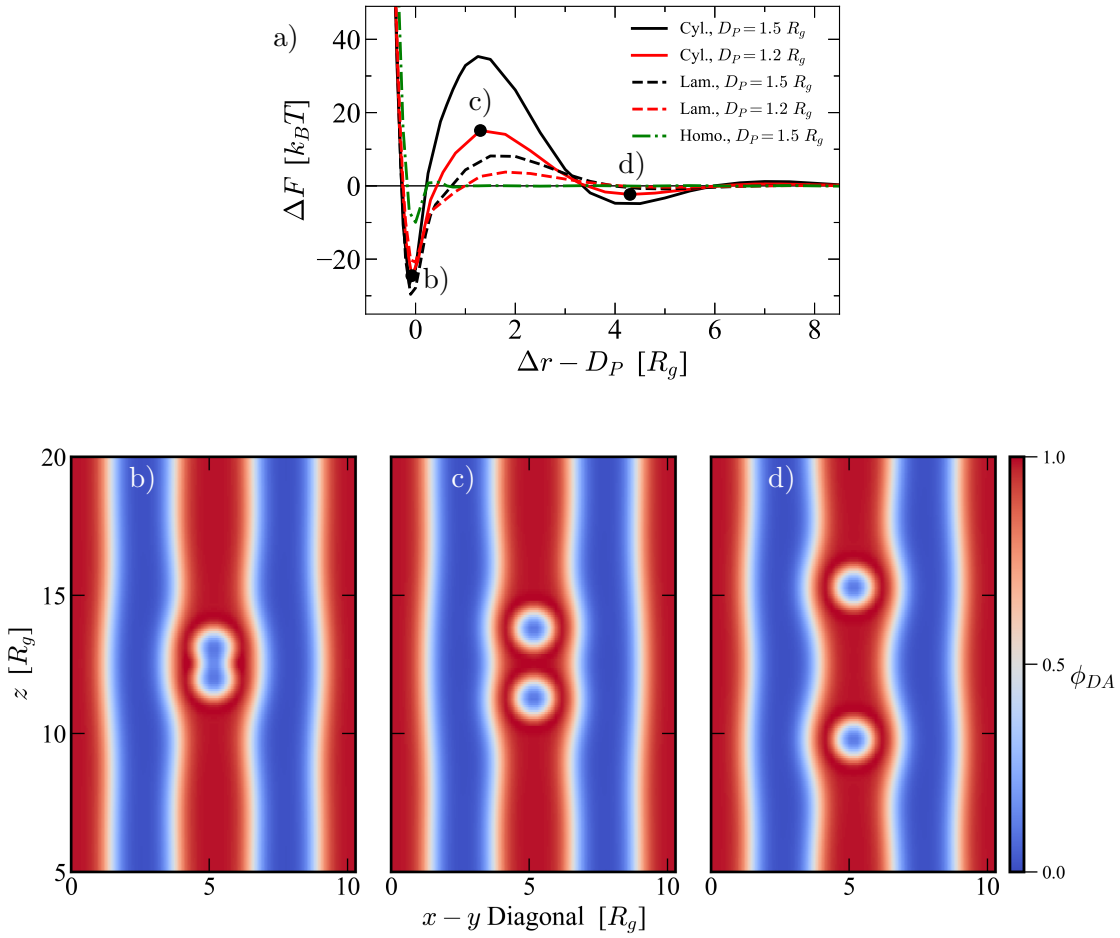

Figure 8: a) Constrained PMFs for 1.5 R_g diameter particles (black lines) and 1.2 R_g diameter particles (red lines) in cylindrical (solid lines) and lamellar (dashed lines) diblock domains. Black circles denote primary minimum, energy barrier, and secondary minimum at -0.075, 1.3, and 4.3 R_g. b), c), and d) show A segment volume fraction in diagonal slices through simulations with 1.2 R_g diameter particles whose surface separation distances are -0.075, 1.3, and 4.3 R_g, respectively. Red regions represent high A segment volume fraction, while blue regions represent low A segment volume fraction.

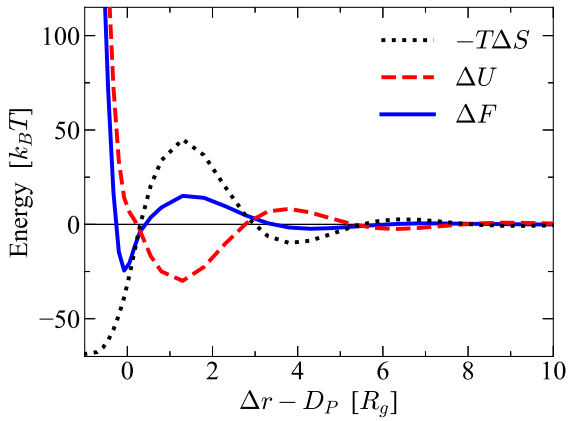

Figure 9: Entropic (black) and enthalpic (red) contributions to the free energy (blue) for 1.2 R_g diameter NPs in a cylindrical diblock domain as a function of distance between NP surfaces

of such a bulge around a large particle contained in a chemically similar diblock domain has been shown in SCFT simulations in work by Matsen and Thompson [63].

The presence of an energy well at point b) is likely due to depletion-attraction interactions, an entropic effect, but the mechanisms underlying the formation of the energy barrier and energy well at points c) and d), respectively, are not immediately apparent. For example, in Figure 8 b), the increase in curvature in the A-B interface could increase the volume of the interface relative to infinite separation, causing an increase in ΔU, the enthalpic contribution to ΔF. Alternatively, increased chain stretching near the defect could increase $-T\Delta S$, the entropic contribution the ΔF. In order to determine how entropic and enthalpic effects contribute to the free energy, the free energy is separated into its enthalpic and entropic components using equations 2.45 and 2.46, respectively. Figure 9 shows the enthalpic (red dashed) and entropic (black dotted) contributions along with the free energy for $D_P = 1.2R_g$. The features in ΔF represent a balance of ΔU and $-T\Delta S$, although features in $-T\Delta S$ generally have a higher magnitude in this case except for the region where $\Delta r - D_P < 0$.

The unconstrained PMFs are calculated by relaxing the centerline constraint on the NPs. Figure 10 shows these unconstrained PMFs for both 1.5 and 1.2 R_g diameter NPs using

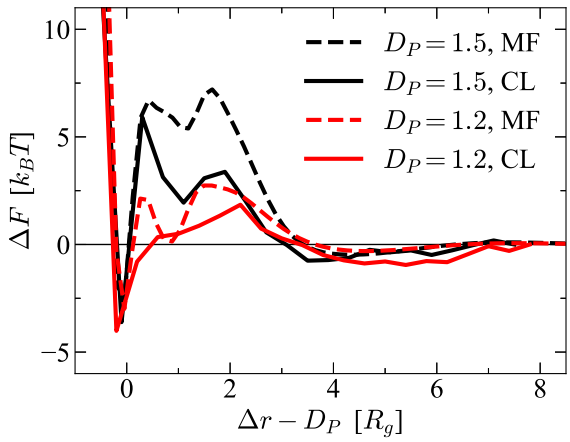

Figure 10: Unconstrained PMFs for 1.5 R_g (black) and 1.2 R_g (red) diameter NPs in a cylindrical diblock domain using MF (solid) and CL (dashed) simulations

both MF and CL simulations. Without the centerline constraint, the features in the unconstrained PMFs have magnitudes that are smaller by a factor of about 5 compared to the corresponding constrained PMFs in Figure 8. Another key difference in the constrained and unconstrained PMFs is the presence of a local minimum at $\Delta r - D_P = D_P(\sqrt{3} - 1)$ in Figure 10 ($\sim 0.9\ R_g$ and $\sim 1.1\ R_g$ for 1.2 R_g and 1.5 R_g diameter particles, respectively). These minima correspond to the distance between second nearest neighbor particles in an HCP lattice. They arise because field-based particles allow for multi-particle correlations. Note that the CL simulations, which sample thermal fluctuations, exhibit similar features as the MF simulations, with the exception of the local minimum from the multi-body effect in the smaller particle size. Because of the good qualitative agreement between MF and CL simulations, only the MF results are presented in the remainder of this article.

Because interactions between the NPs and the A-B interface are important, the effect of quench depth (χN) on the PMF is explored next. Recalling that the order to disorder transition (ODT) occurs at $\chi N = 10.5$ for the standard diblock model [4], the unconstrained PMFs at moderate ($\chi N = 30$) and strong ($\chi N = 60$) segregation were compared, as shown in Figure 11 a). Both PMFs represent cylindrical systems with particles of diameter 1.2 R_g. A-segment density maps along the diagonal of these simulation boxes can be seen in Figure

11 b) and c). The increased A-B repulsion in the $\chi N = 60$ simulation led to less deformation of the A-B interface (i.e. lower curvature), which in turn leads to a lower energy barrier to bring 2 NPs into contact. The relatively undeformed interface between the cylindrical domain (red) and the matrix (blue) at $\chi N = 60$ partially explains why bulging, to our knowledge, has been difficult to observe in experiments [16, 51]. Typically, BCPs have large χN (> 30) which ensures strong microphase separation and a high free energy penalty to perturb the A-B interface. In addition, experiments typically use particles with diameters that are much smaller than the size of the diblock domain. Experiments by Warren and coworkers [89] have shown that particles with diameters larger than a certain threshold tend to disrupt the diblock structure to form onion-ring structures. For a PI-*b*-PEO diblock with silica NPs, the threshold was found to be the root-mean-square-end-to-end distance of the PEO block, which formed the diblock domain containing the NPs [89]. Combined, these factors suggest that bulging of a diblock domain due to incorporation of particles occurs over a narrow range of parameters. However, as shown in Figure 11, non-negligible particle-particle interactions are still seen even with barely visible bulging, which again emphasizes that entropic effects play a substantial role in the interactions.

After showing that diblock domains can increase the strength of effective interactions between particles, simulations were performed to determine whether this effect holds as particles chain together to form longer aggregates. These simulations contained 1, 2, or 3 co-linear, fixed NPs within a cylindrical domain and computed the unconstrained PMF from each relative to one of the outermost chained particles. In each simulation, $D_P = 1.2\ R_g$ and $\chi N = 60$ and the explicit particles are each placed in a chain with particle centers a distance of 1 D_P from adjacent particles. Figure 12a) shows how the PMF curves change as a function of NP chain length. Figures 12b-d) show A-segment volume fraction in 2D slices along the diagonal of the 3D simulation boxes associated with the 1, 2, and 3 fixed particle curves, respectively. There is a small increase of about 0.1 k_BT in the larger of the two energy barriers for a particle to join a chain of 2 particles compared to joining a single particle, but a negligible difference when a 3rd particle is added to the chain. This

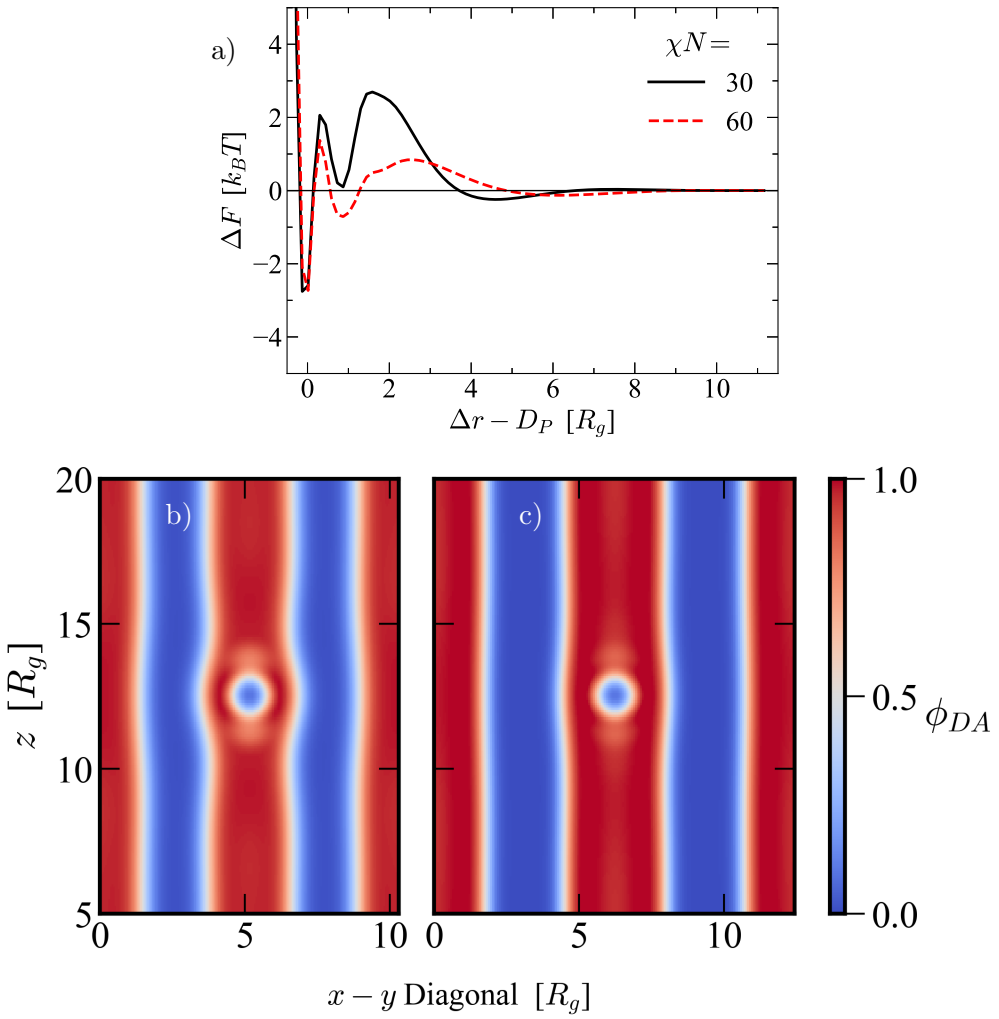

Figure 11: a) Unconstrained PMF for cylindrical A-B diblock system with particles of diameter 1.2 R_g at 2 different A-B repulsion strengths. b) and c) show A-segment volume fraction in 2D slices through the diagonals of the simulation boxes for $\chi N = 30$ and $\chi N = 60$, respectively.

observation suggests that rod-like NPs can be fabricated using chains of spherical NPs. This is a very attractive approach because spherical NPs are more readily available and easier to synthesize with monodisperse sizes at low polydispersity [34].

To better understand how the microphase-separated polymer structure affects chain stretching and alignment, the nematic order parameter was calculated to quantify local chain alignment in diblock and homopolymer simulations. Figure 13a) shows visualizations of the nematic order parameter $S_{xx}(\mathbf{r})$ within x-z slices through the particle center. Larger values (deeper red) correspond to stronger alignment in the x-direction (horizontal), while smaller values (deeper blue) correspond to stronger alignment in orthogonal directions. To see how the patterns correspond to the locations of the diblock domains, 13b) contains a map of diblock A volume fraction from the same slice as the $\Delta r - D_P = 11.2\ R_g$ simulation from 13a). Similar to what was found in Prasad et al.[68], far from either NP, these plots show nematic order of 0 at the center of each domain due to symmetry, negative values at the interface between domains, and positive values everywhere else. The patterns immediately around the particles are consistent with polymer chains laying flat against the particle surface, as illustrated in the schematic of polymer conformations near the particle in Figure 13d). In fact, these patterns are seen with nearly identical magnitudes in pure homopolymer simulations as well. To focus on how the presence of the diblock affects conformations, the nematic order parameter from corresponding homopolymer simulations is subtracted from 13a) to get S_{xx}^{res} shown in 13c). Analysis of the residual nematic order shows that chains in the neighboring B domain near the particle are compressed, illustrated in the schematic in 13d). In contrast, the layering of the chains in the immediate vicinity of the NP surface is absent in 13b), suggesting this affect is the same as in the homopolymer. The strength of the compression in the nearby B domain appears to change subtly as a function of particle surface-to-surface distance. To quantify this subtle changes, line plots were taken along the x-axis through the center of the lower particles in 13e). The largest changes occur near $x = 1.14$ and $x = 4.0$ in these plots. Choosing $x_m = 1.14$ and plotting the residual nematic order from this x-value in 13f), the residual nematic order parameter is inversely correlated

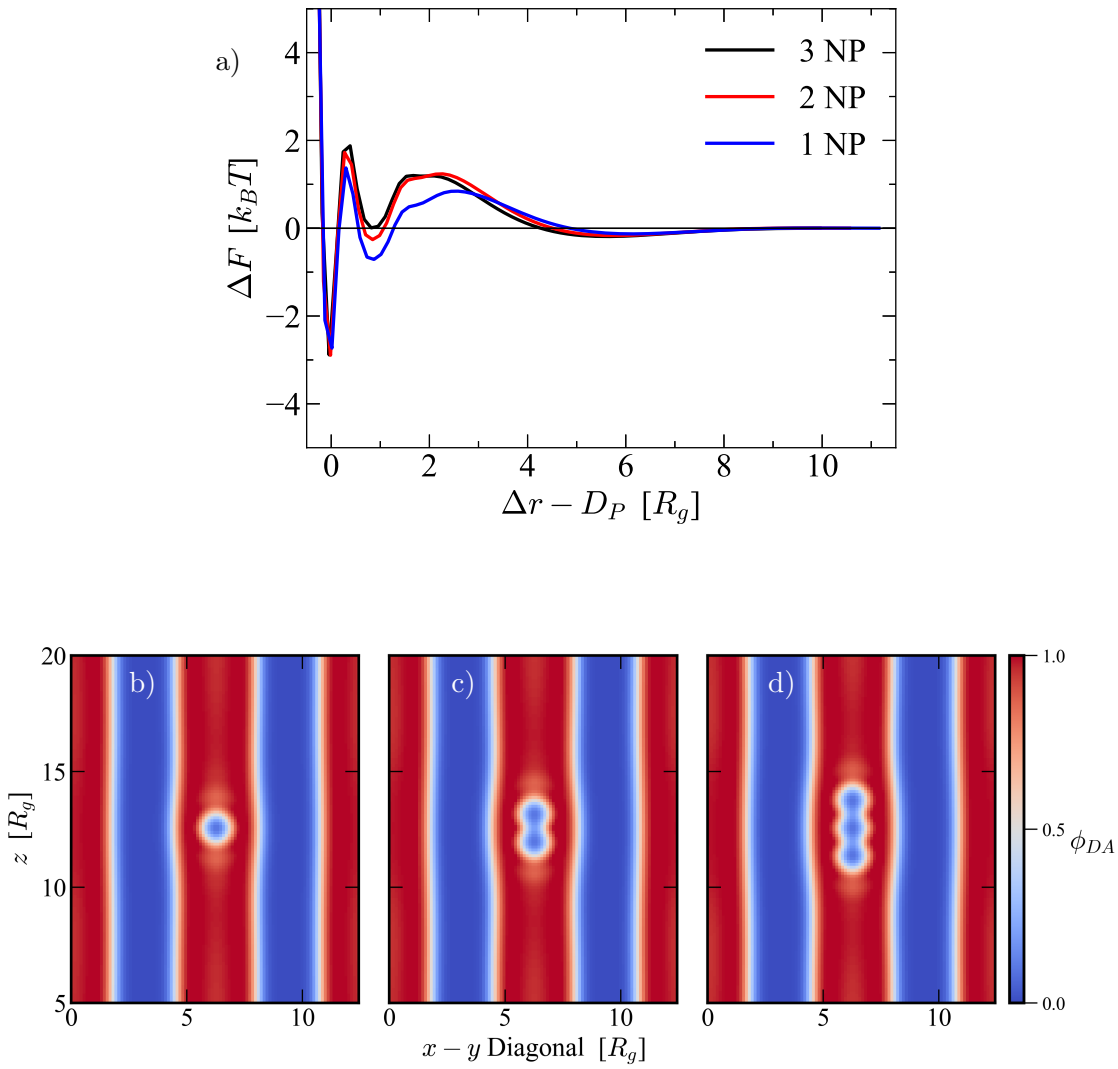

Figure 12: a) Unconstrained PMFs for strings of b) 1, c) 2, or d) 3 fixed, explicit NPs with diameter $D_P = 1.2\ R_g$ along the Z-dimension within a cylindrical diblock domain.

to the first energy barrier and second local minimum of the associated free energy curve, which would correspond to a direct correlation between $-T\Delta S$ and the same features. This suggests that chain compression in the neighboring B domain has some mid-range effects on the free energy.

4.3.2. Grafted Nanoparticles

Next, the effects of polymer brushes on the interactions between NPs were investigated. Simulations with long and short brushes were performed with $N = 60$ and $N = 6$, respectively. For both systems, $D_P = 0.6\ R_g$, $\sigma = 20\ R_g^{-2}$, and $P = 60$. Thus, the brushes correspond to the wet ($P/N = 1$) and dry ($P/N = 10$) brush limits in homopolymer matrices respectively. Figure 14 shows the constrained PMFs for the wet (black) and dry (red) brush cases. Comparing these PMFs to those for the bare particles, the first local minimum in ΔF has shifted by a distance that scales approximately with $\sqrt{N}$, consistent with Gaussian conformations of the brush. For $P/N = 10$, the first local minimum is also a global minimum, similar to bare particles. However, for $P/N = 1$, because of steric hindrance of the wetted chains, that first local minimum is not the global minimum, and the equilibrium separation distance is instead around 6.5 R_g.

The brush and A block domain density profiles for the $P/N = 1$ and 10 systems were determined to help inform further analysis of this system. Figure 15a) shows the diblock A volume fraction in an $x - z$ slice through the center of a fixed particle in a $P/N = 1$ simulation and labels the radial and axial directions for reference. Figures 15b) and c) show the brush and A block domain profiles in the radial and axial directions from a particle center, respectively. The short grafted chains of the $P/N = 10$ system have very similar density profiles (i.e., symmetric) in both the radial and axial directions, suggesting that the A-B interface does not have a strong influence on brush conformation in that case. The longer grafted chains with $P/N = 1$, however, have a radial density profile that is shorter than the axial profile, extending about half the distance due to influence of the A-B interface. Frischknecht and coworkers previously computed brush profiles from simulations

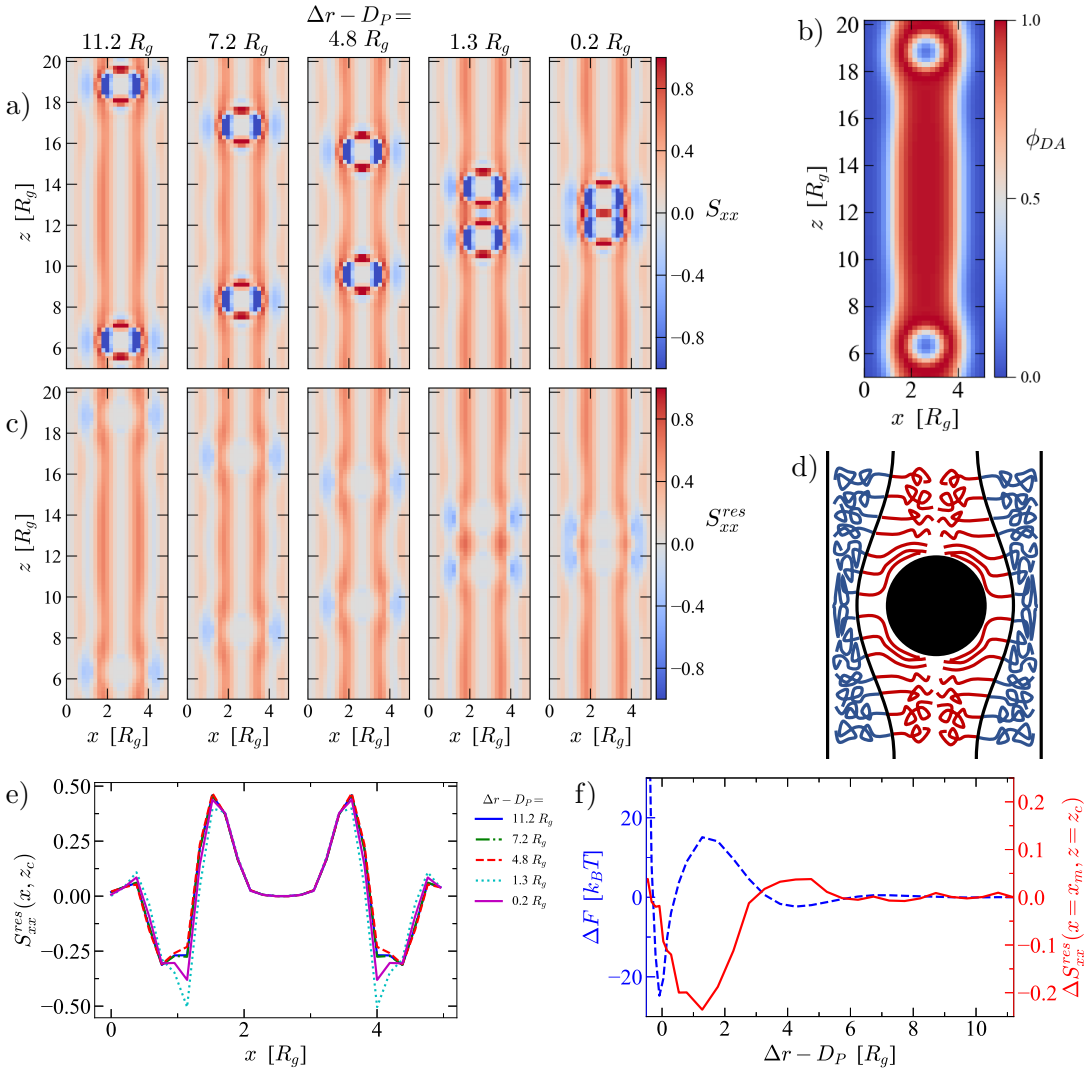

Figure 13: a) S_{xx} maps in $x - z$ slices through the center of the lower half of the simulation box for various particle surface-to-surface distances ($\Delta r - D_P$). All simulations here are for $D_P = 1.2\ R_g$. c) Diblock A segment volume fraction map in $x - z$ slice corresponding to the 11.2 R_g nematic order slices in a) and b) for reference. b) S_{xx}^{res} maps for the same simulations as a). d) Schematic of polymer stretching and compression near a particle. e) S_{xx}^{res} profiles along the x-axis through the center of the lower particle for each simulation in a). f) Constrained PMF (dashed blue line) plotted against residual nematic order parameter values (solid red line) at the A-B interface next to the particle ($x = 1.14$) as a function of particle-particle surface separation distance.

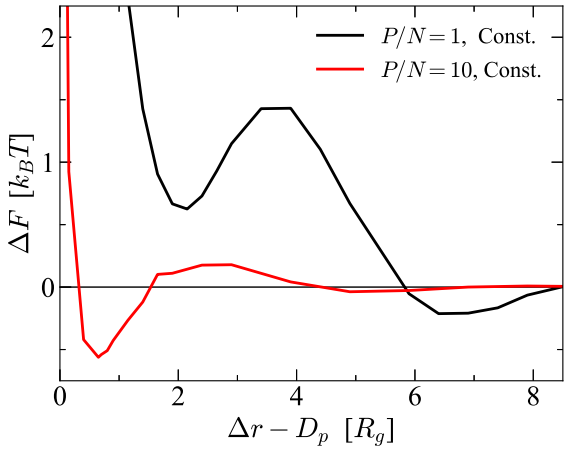

Figure 14: Constrained PMFs 0.6 R_g diameter NPs where $P/N = 1$ (black) and $P/N = 10$ (red)

of polymer grafted gold nanorods in a homopolymer matrix [21] with the x-axis normalized by ideal radius of gyration of the brush rather than the matrix, and the results presented here are in good qualitative agreement with the lone exception of the radial direction in the $P/N = 1$ case. Polymer chain alignment in the grafted systems was also investigated by calculating residual nematic order as was done for the bare NPs (not shown). Overall, the changes in the matrix chain conformations as the particles were brought together were minimal as the grafts effectively screened the conformational changes.

Similar to the bare particles case, the enthalpic and entropic contributions to the changes in the free energy as the grafted particles are brought together can be analyzed. Figures 16a) and b) show these contributions for $P/N = 10$ and $P/N = 1$, respectively. For $P/N = 10$, the first local minima for both the entropic (dotted black) and enthalpic (dashed red) curves are less than 0, leading to a net weak attraction between the particles. However, for $P/N = 1$ in Figure 16b), in the region $\Delta r - D_P < 4R_g$, where significant brush layer overlap occurs, the entropic component is significantly higher, increasing the free energy even at the local minimum. This can be explained by the loss of conformations available to the grafted chains as the brush layers overlap. Additionally, the features in the enthalpic component have a higher magnitude in the $P/N = 1$ case because of the stronger deformations in the

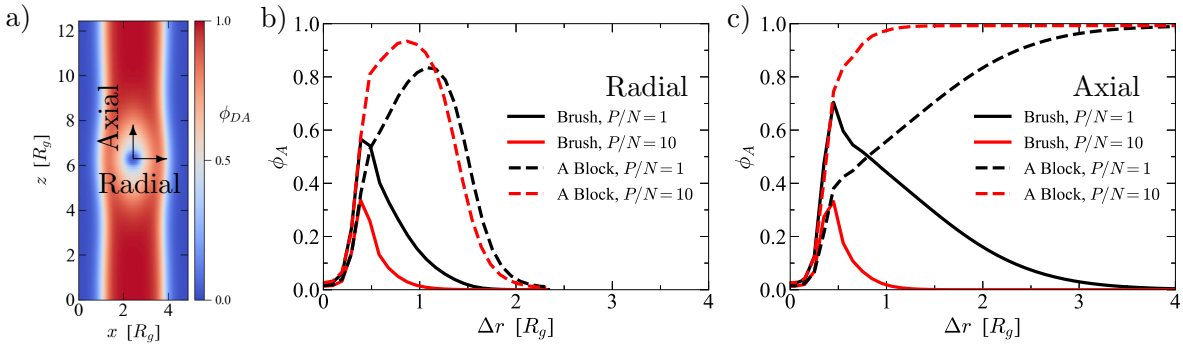

Figure 15: a) Diblock A volume fraction map in $x-z$ slice through center of particle in a $P/N = 1$ simulation. Radial and axial directions are labelled for reference. b) A-segment density profiles in the radial direction from a particle center. c) A-segment density profiles in the axial direction from a particle center. Both graphs plot brush (solid) and A block domain (dashed) profiles for $P/N = 1$ (black) and $P/N = 10$ (red).

A-B interface due to the thicker brush layer.

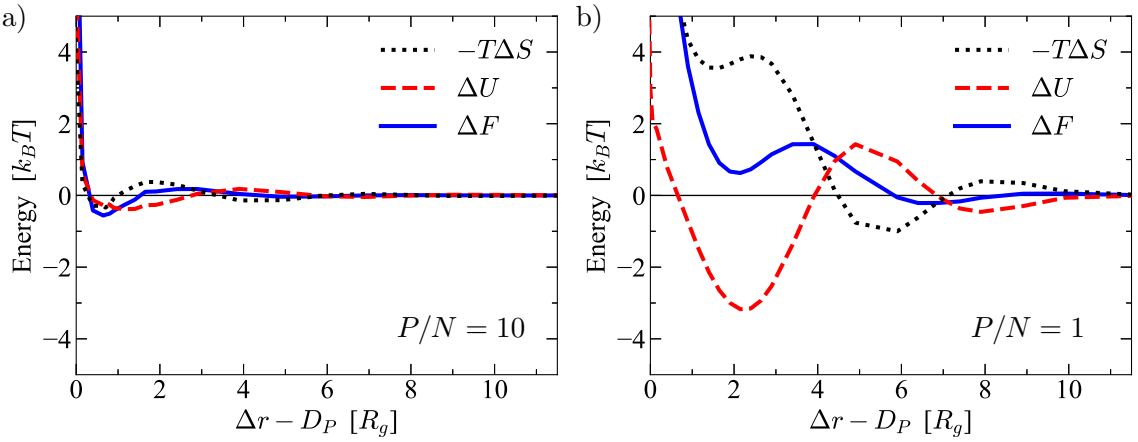

Figure 16: Entropic penalty (black), potential energy (red), and free energy (blue) for constrained systems with a) $P/N = 10$ and b) $P/N = 1$ for 0.6 R_g diameter particles in a cylindrical diblock domain as a function of distance between particle surfaces

The enthalpic component can further be broken down into contributions from diblock and brush chains. To decouple potential energy into brush and diblock contributions, an alter-

native method to measure potential energy is employed using

$$U_D = \frac{\chi}{\rho_0} \int d\mathbf{r} \rho_{A,c,diblock}(\mathbf{r}) \rho_{B,c}(\mathbf{r}) \tag{4.1}$$

$$U_G = \frac{\chi}{\rho_0} \int d\mathbf{r} \rho_{A,c,grafts}(\mathbf{r}) \rho_{B,c}(\mathbf{r}). \tag{4.2}$$

Figure 17 a) shows U_D and U_G, as well as their sum. As expected, $U_D + U_G$ (blue) matches very closely to Equation 2.45, with the only significant difference being a lower value near $\Delta r - D_P = 0$, when the particle cores are in contact. Comparing the magnitudes of the two components, it can be seen that the features in the potential energy curve are primarily driven by contact between diblock A and B segments. Figure 17 b)-d) show the diblock A density at different particle separation distances. In all three density maps, bulging can be seen in the A-B interfaces around the particles. In Figure 17 b), potential energy is at a minimum because the bulges merge to form relatively flat interface. In Figure 17 c), potential energy is higher due to increased interfacial area since the bulges are beginning to separate, producing more interfacial area and curvature. In Figure 17 d), potential energy is approaching a constant value because the bulges are too far apart to have meaningful interactions.

Finally, the effect of grafting density on the unconstrained PMFs are studied. Figure 18 shows unconstrained PMFs for 0.6 R_g diameter NPs with graft densities of 40, 20, and 10 R_g^{-2}. For reference, given PS-*b*-P2VP with $M_n = 177$ kg/mol and a NP with a grafted brush having $M_n = 25.5$ kg/mol, a graft density of $\sigma = 10/R_g^2$ corresponds to approximately 0.55 chains/nm^2. Figure 18 shows that the magnitudes of the energy barriers and wells increase linearly with increasing graft density. This suggests that the strength of NP interactions can be tuned by adjusting the graft density. Increasing the graft density increases the effective particle size, which increases deformation of the A-B interface, similar to increasing the core diameter of the NP.

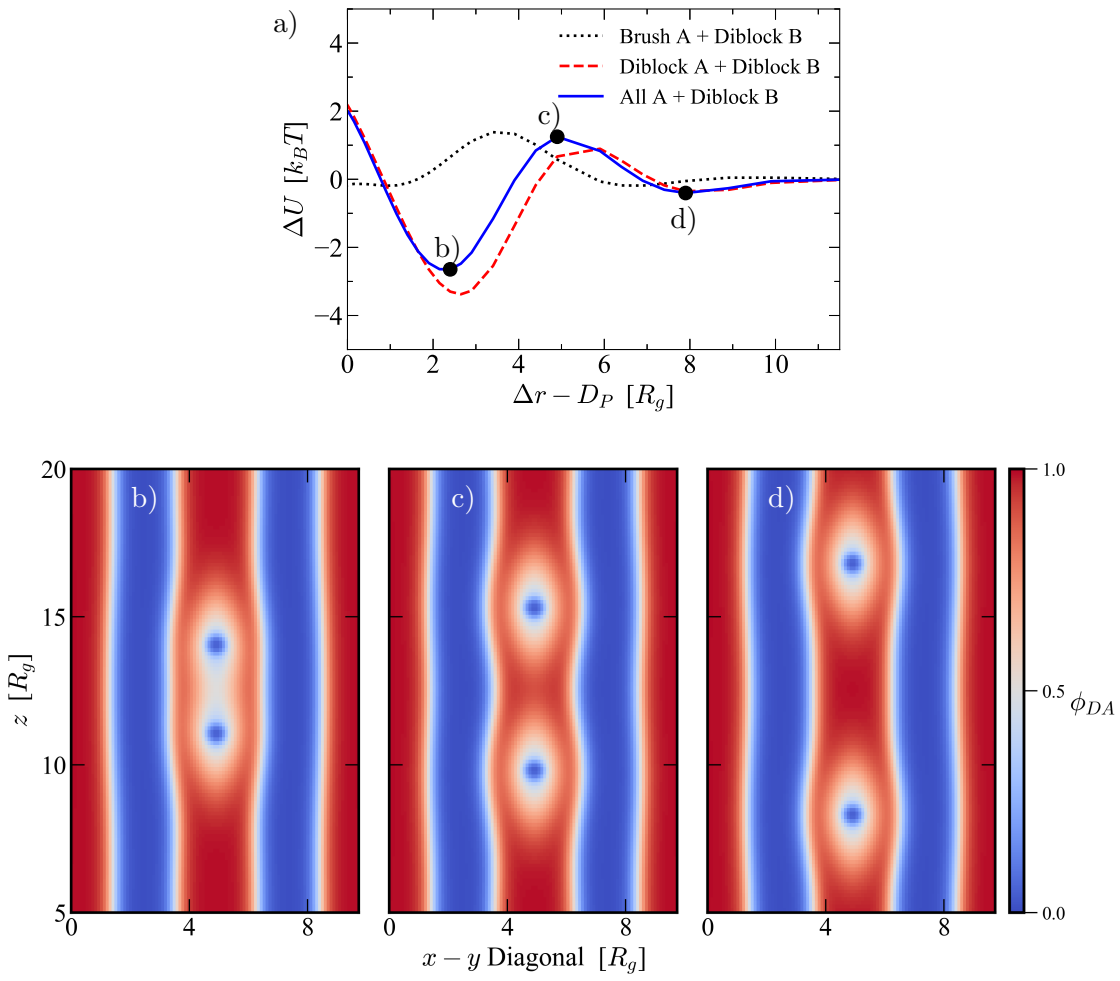

Figure 17: a) A-B contact potential between graft A and diblock B, and diblock A and diblock B b), c), and d) show diblock A segment density in diagonal slices through simulations with 0.6 R_g diameter particles with A grafts such that $P/N = 1$ whose surface separation distances are 2.4, 4.9, and 7.9 R_g, respectively. Red regions represent high A segment density, while blue regions represent low A segment density.

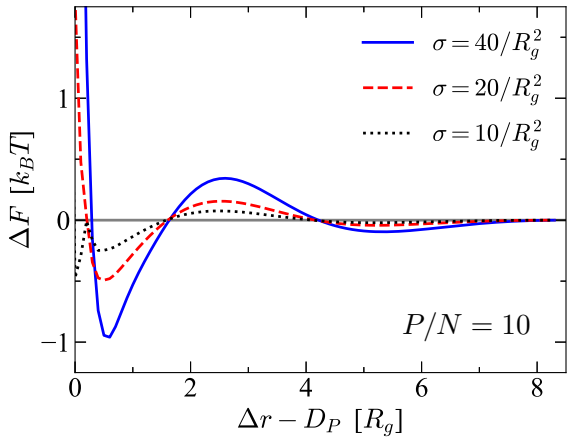

Figure 18: Unconstrained PMFs for 0.6 R_g diameter NPs in cylindrical diblock domains with graft densities of 40 (blue), 20 (red), and 10 (black) chains/R_g^2

4.4. Conclusions

In this chapter, the interactions between bare and grafted NPs in diblock copolymer domains were quantified. Systems in which the particle diameter was similar to the width of the BCP domain in which the particle was located were studied with field-theoretic simulations. Although bare particles in contact exhibit a global energy minimum, chain stretching and compression in the diblock chains can create an energy barrier on the order of several k_BT. This suggests that the ratio of chained particles to free particles could be tuned by changing the size of the particle relative to the width of the diblock domain. For systems with grafted particles, on the other hand, the interactions between the particles are governed by a more nuanced interplay between entropic and enthalpic effects. The equilibrium separation between particles can be tuned by controlling P/N, and the strength of the energy well and energy barrier can be tuned by controlling the graft density.

This control over inter-particle spacing could be useful in several applications. For example, NPs could be arranged in a chain along the axis of a cylindrical diblock domain, allowing for improved thermal or electrical conductivity, or finely-tuned optical properties. The energy barrier, which is especially strong for bare particles, could be exploited to lock in particle chaining. If temperatures are increased high enough for particles to overcome that energy

barrier, or some other method is used to temporarily reduce or overcome the barrier, the particles are unlikely to escape the globally stable energy well. An application like this could allow an alternative to dispersing nanorods into cylindrical domains, which is difficult experimentally. This could open up new techniques for fabricating materials with directed properties.

CHAPTER 5 : Spherical Nanoparticles with Attractive Particle-Polymer Interactions

5.1. Introduction

Polymer nanocomposites (PNCs) are a promising class of materials with a wide variety of potential applications. By dispersing nanoparticles into polymers, many types of property enhancements can be achieved, including mechanical [64], optical [34, 5], thermal [90], and electrical [22] properties. Controlling dispersion state of particles and the interactions between particles is critical to achieving desired properties. For example, Moll et al. demonstrated that the mechanical strength of a PNC depends on the structure of the particle aggregates that form, with a networked particle structure leading to the highest strength [64]. Genix et al. found that because of the different ways short and long matrix chains can mediate interactions between particles, an optimal matrix size can be found for a given type of bare nanoparticle that will maximize the shear modulus. One method for influencing the particle dispersion state is by modifying the surface chemistry of the particles using short ligands [69, 51]. By tuning the surface density of the attached ligands, the strength of effective particle-polymer attraction should be able to be varied over a continuous range.

Previous work by Hall and Schweizer used the polymer reference interaction site model (PRISM) to study the effect of the particle-polymer attraction strength on the dispersion state of particles [27]. They found that in an athermal PNC, particles would aggregate, as expected, and that increasing the particle-polymer attraction strength would allow particles to disperse. They also found a counterintuitive effect where particles would return to an aggregated state with a high enough particle-polymer attraction strength, due to polymer-mediated bridging of particles. They produced a phase diagram delineating which combinations of particle-polymer attraction strength and particle volume fraction would lead to miscible states and which would lead to aggregated states. This phase diagram showed that as volume fraction increased, the range of particle-polymer attraction strength

in which a miscible state occurred decreased. While PRISM is a powerful tool for efficiently generating phase information, it has some limitations. As a liquid state theory, it only has access to radially averaged pair pair correlation function and structure factor information. Additionally, it only has access to single phase regions, so it can't probe regions where phase coexistence occurs.

Phase diagrams such as these are a common way to understand and predict dispersion state of PNCs from a few key variables. Many experimental and simulation efforts have made phase diagrams for this purpose [27, 53, 50, 95] and they have been shown to be a powerful tool. However, phase diagrams don't tell the whole story about particle clustering behavior. Koski, Ferrier, and Krook have taken preliminary steps to understand phase behavior in situations with partial clustering but not complete aggregation [50]. In this work, the clustering behavior of particles in PNCs is measured more quantitatively. We show that clustering behavior changes more slowly as a function of key variables than a phase diagram lets on. Furthermore, we show that even within a particle-rich phase, cluster structure can change as a function of attraction strength.

5.2. Numerical Methods

Simulations of bare nanoparticles were performed using the TILD method described in 2.2.1. Polymer chains were discretized into $P = 20$ segments. Particles were simulated with parameters $\kappa = 25$, $\sigma_P = \sigma_{LJ} = 1\ R_g$, and $\xi_P = 0.2\ R_g$. For phase diagram simulations, a simulation box with dimensions $10\ R_g \times 10\ R_g \times 40\ R_g$ was used with $45 \times 45 \times 175$ collocation points used for grid-based operations. Simulations were run and analyzed as described in Section 2.2.3. Particle-polymer attraction ϵ, was varied from 0 to 6 k_BT at particle volume fractions ϕ_P ranging from 0.05 to 0.15. For each ϵ, the simulation with a final volume fraction of the particle-rich phase (if it exists) closest to 0.5 was used for phase diagram generation. For cluster analysis simulations, a simulation box with dimensions $8\ R_g \times 8\ R_g \times 8\ R_g$ was used with $63 \times 63 \times 63$ collocation points used for grid-based operations. Simulations were run and analyzed as described in Section 2.2.4. ϵ, was again

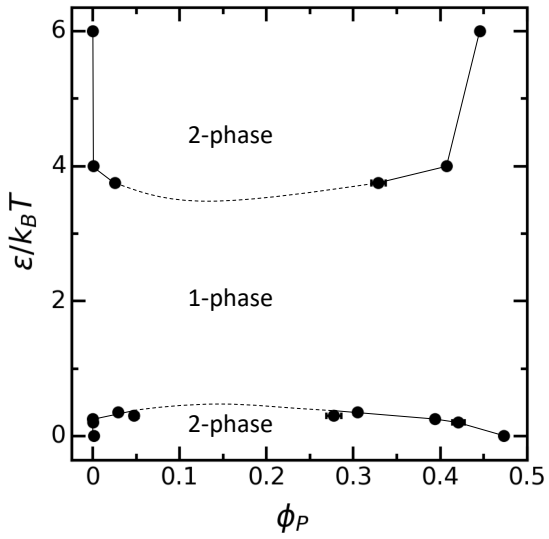

Figure 19: Phase diagram for $\sigma_P = 1.0\ R_g$ particles as a function of ϕ_P and ϵ.

varied from 0 to 6 k_BT at particle volume fractions ϕ_P ranging from 0.05 to 0.15.

5.3. Results and Discussion

In order to get a preliminary understanding of particle dispersion and aggregation behavior with particle-polymer attractions, a phase diagram, seen in Figure 19, was generated as described in Section 2.2.3. This diagram can be qualitatively compared to those produced by Hall and Schweizer using the PRISM model [32]. Note that while ϵ is also used in this work to encode the strength of polymer attraction at the particle surface, the shape of the attractive well in the pair potential differs between the two studies. Despite the model differences, the phase diagrams here show qualitative agreement with the PRISM-generated phase diagrams. In both cases, at low values of ϵ, we see strong macrophase separation. At intermediate values of ϵ, we see no macrophase separation, then at high values of ϵ, we once again see macrophase separation.

The reason for this return to a macrophase-separated state at high enough particle-polymer attraction strength is understood to be mediated by polymer chains "bridging" the gaps between adjacent particles [31, 32, 27]. To verify that this same mechanism was at play

here, the particle-polymer (g_{AP}) and particle-particle (g_{PP}) pair correlation functions were examined. Figure 20 shows $g_{PP}(r)$ for various values of ϵ used (rows) and for the two different particle sizes (columns) studied. The x-axis is scaled by the particle diameter, $D_P = 2.47\ R_g$, which is determined by the location of the first peak in the $\epsilon = 0$ case. The dashed lines mark $r/D_P = 1.125$, which is used as a cutoff distance for clustering analysis, which will be discussed below. At low and high values of ϵ, a sharp first peak is seen, indicating many particle-particle contacts. If polymer-mediated bridging explains the return to phase separation in the high ϵ regime, we would expect the first peak in the higher ϵ regime to be shifted slightly to the right to accommodate monomers between neighboring particle surfaces. We do in fact see a slight right shift of about $0.25a$ where a is the smearing length scale used in Equation 2.6. The fact that the shift is less than a full monomer diameter can be explained by the use of "soft" potentials rather than hard-sphere potentials.

The polymer-particle distribution functions, g_{AP}, shown in Figure 21, provide further evidence for polymer bridging. The x-axis is scaled by the particle radius, R_P, defined as $R_P = D_P/2$. For all cases, there is an expected peak at $r = R_P$, corresponding to increased polymer density at the particle surface. With increasing ϵ, the magnitude of that peak increases, suggesting an increased amount of polymer available to bridge particles.

After seeing qualitative agreement with expected phase behavior, we sought to quantitatively determine what particle clustering looks like. We first measured how cluster sizes changed over time, using the cluster definition described in Section 2.2.4. Figure 22 shows the cluster size distribution evolution over time for simulations where $\phi_P = 0.15$. Each point contains information about the number of clusters of a particular size found in a particular iteration of the simulation. For example, a large point at a y-value of 1 means there were many clusters with cluster size of 1 (i.e. a lone particle), and a small point at a y-value of 103 means that all 103 particles were part of 1 single cluster. Each plot shows that equilibration is reached within about 1 million iterations. Intermediate values of ϵ

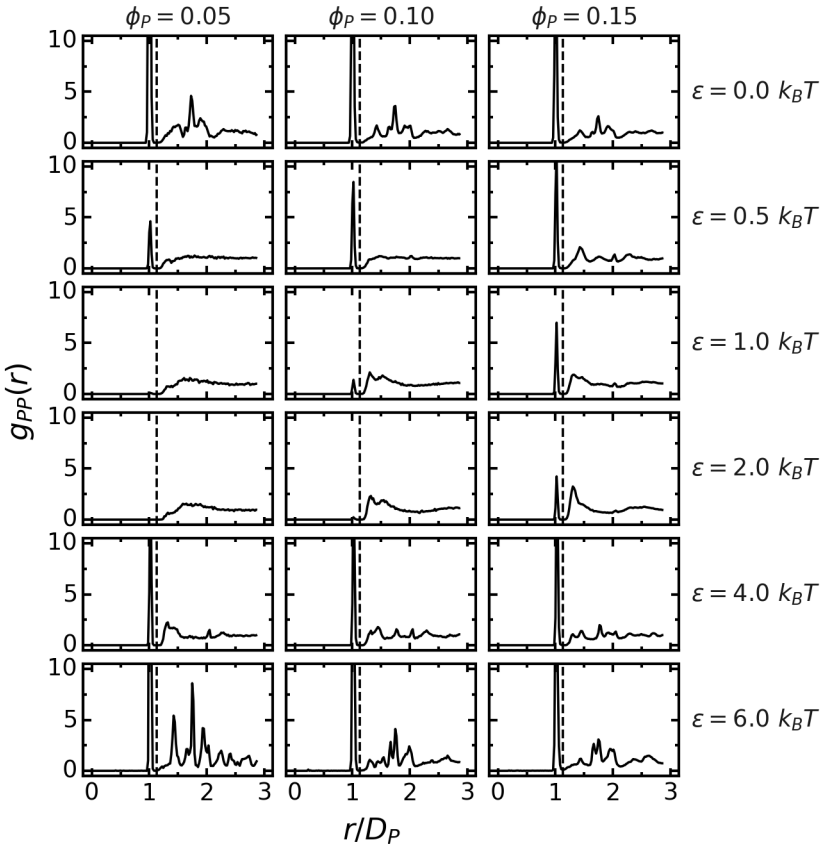

Figure 20: Particle-particle pair correlation functions for the purely repulsive ($\epsilon = 0\ k_BT$) to the strongly attractive ($\epsilon = 6\ k_BT$) from top to bottom. The left-to-right columns show increasing particle volume fraction.

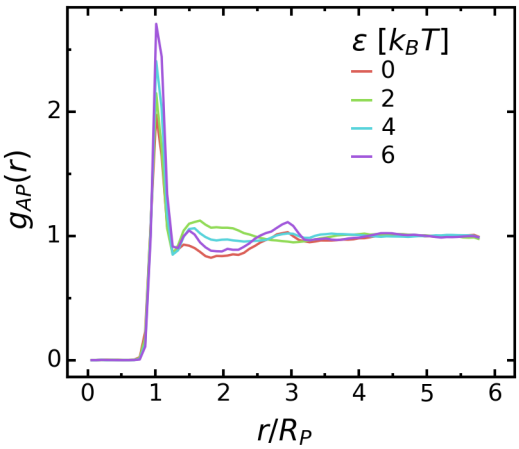

Figure 21: Particle-polymer pair correlation function, showing the inscrease in intensity of the first peak as ϵ increases.

leads to smaller cluster size on average, while small and large values of ϵ lead to all particles joining the same cluster.

By aggregating cluster size information from the last 250,000 iterations of each of these and other $D_P = 2.47R_g$ simulations, we get a more nuanced perspective on what clustering looks like around the phase boundaries. Figure 23 shows these equilibrium cluster size distributions as a function of ϕ_P and ϵ. Rather than seeing a perfectly sharp transition from fully clustered to fully miscible, there's a transition period of roughly 0.5 k_BT where we see coexistence of intermediate-sized clusters with disconnected particles. The plot for each value of ϕ_P has a dashed line showing the mean cluster size as a guide to the eye. Looking at both the dashed lines and the actual cluster size points as ϕ_P increases, we see the miscible window decrease, as expected.

We also wanted to better understand how cluster structure changes as a function of ϵ and ϕ_P in these systems. We used the particle coordination number as a measure of this. High coordination numbers correspond to densely packed particle clusters while low coordination numbers correspond to more loosely packed clusters or clusters with high surface area to volume ratio. Figure 24 shows coordination number distributions from the last 250,000

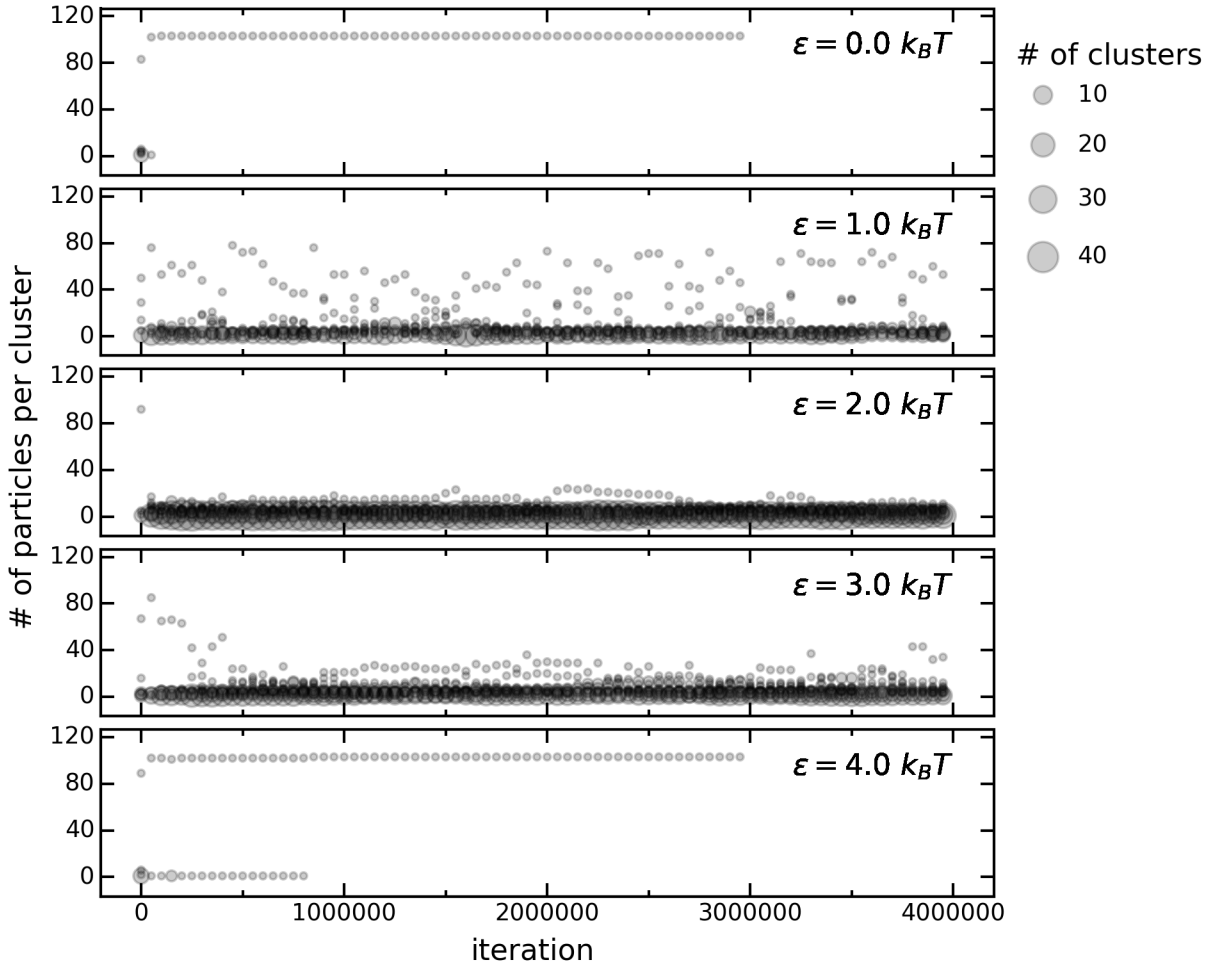

Figure 22: Cluster size distribution as a function of time. Each chart comes from a $\phi_P = 0.15$ simulation with a different value of ϵ. Each point represents a particular cluster size at a particular iteration. The size of each point represents the number of clusters of that size.

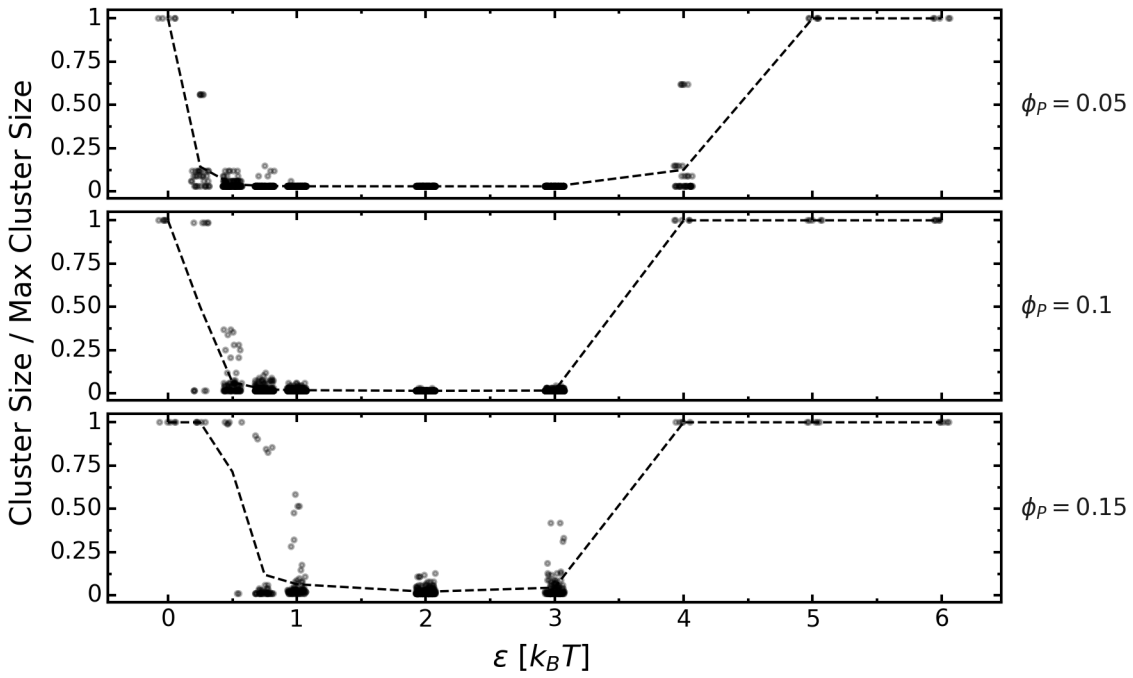

Figure 23: Cluster size distribution from last 250,000 iterations of simulations with $\phi_P = 0.05$ (top), $\phi_P = 0.1$ (middle), and $\phi_P = 0.15$ (bottom) on a range of ϵ values from 0 to 6. Dashed line represents mean cluster size for a given ϵ and ϕ_P.

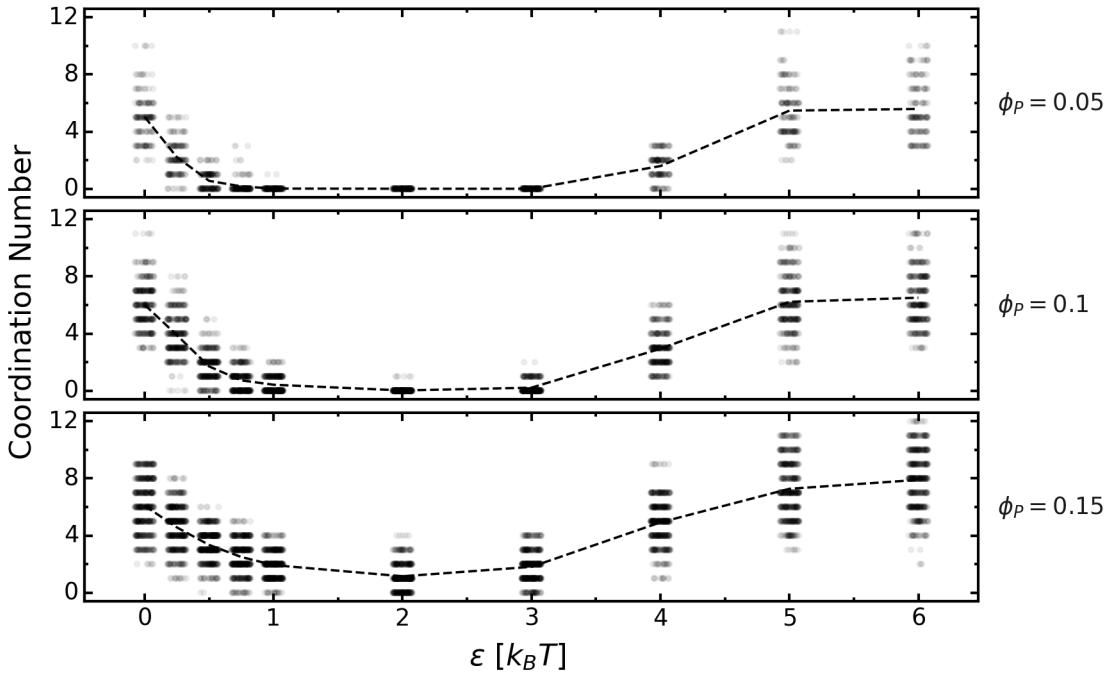

Figure 24: Coordination number distribution as a function of ϵ and ϕ_P. Each point represents a single particle from one of the last 5 simulation frames saved with 50,000 iterations between each iteration. The dashed lines represent the mean coordination number from those 5 frames.

iterations of simulations, and is structured in an analogous way to Figure 23. For all three volume fractions, the coordination number distribution changes more slowly as a function of ϵ than does the cluster size distribution. Even within the fully aggregated systems where $\phi_P \geq 0.1$ and $\epsilon \geq 4k_BT$, the coordination number distribution continues to increase as a function of ϵ. This taken together with the cluster size distribution results suggest that by tuning the particle-polymer attraction strength, it could be possible to target different cluster sizes and cluster densities.

5.4. Conclusions

In this chapter, clustering behavior of PNCs with attractive particle-polymer attractions was quantified. First, a phase diagram was generated to ensure results qualitatively aligned with prior work. Next, cluster sizes and structures were measured to gain a more in-depth

look at the real clustering behavior. Both cluster size distribution and coordination number distribution data show a more nuanced view of the system, demonstrating that 1) even in a miscible system, small clusters can form, and that 2) cluster size and structure change more slowly than is apparent from a phase diagram.

These insights show that, while phase diagrams are powerful tools, they don't tell the whole story. Tuning the particle-polymer attraction strength and particle volume fraction could allow experimentalists to target different cluster size distributions and cluster structures, depending on the desired application.

CHAPTER 6 : Conclusion and Outlook

In Chapter 1, we discussed the critical importance of two key effects—anisotropy and aggregation—on the resulting properties of PNCs. The presence or absence of particle clusters, the shape of those clusters, and the isotropy and anisotropy of the polymer in which those particles reside determine properties like mechanical strength, conductivity, permeability, and many other potential properties. The remaining chapters detailed work conducted to explore those effects. Chapter 2 discussed the equilibrium and dynamic polymer field theory methods used throughout the work. These methods have broad applicability and have the potential to explore countless other polymer-based systems in future studies. In Chapter 3, we explored the use of anisotropic nanoparticles—gold nanorods in particular—to bridge vertical cylindrical diblock domains via directed self-assembly. Chapter 4 investigated the potential to employ directed self-assembly towards arranging spherical nanoparticles into chains within cylindrical diblock domains. Finally, Chapter 5 explored the effect of tuning particle surface chemistry on the resulting particle cluster distributions.

This work has the potential to be extended and expanded in several directions that could provide further fundamental and practical insight that could lead to improvements in specialty polymer nanocomposites. The bridging nanorod work could be extended by adding particle entropy and multiple particle interactions into consideration. The work so far assumed fixed particles, so the only entropic contributions to the total free energy came from the polymer, and only one nanorod was included in each simulation. Using TILD with explicit nanorods, especially multiple nanorods and multiple cylindrical domains, would produce a more complete picture of how particles tend to arrange on the surface of the film. This could potentially be done in a 2D simulation to reduce computational cost.

Krook and Tabedzki have already begun to extend the work in Chapter 4 by studying nanoplates in lamellar diblock domains. They found similar interactions shown in this work, and demonstrated close agreement between simulation and experiment. Further extension

of this work could make use of TILD to analyze dynamic clustering of particles of different sizes within diblock domains. On a more fundamental level, there is an open question of the amount of "softening" of nanoparticles when they are treated as field-based rather than explicit, and further simulations of explicit and field-based particles would enable us to quantitatively answer that question.

Finally, for the work on attractive polymer-nanoparticle interactions, work is currently being done to select pair potentials that more closely match experiments. The form of the pair potentials used in this work, especially the particle-polymer pair potential, are fairly crude. Work currently under way is making use of iterative Boltzmann inversion (IBI) to as a more data-driven approach to designing appropriate pair potentials. The results with better pair potentials will likely give qualitatively similar results to those in Chapter 5, but will can be expected to be more quantitatively similar to experimental results. Since the goal is to improve real polymer nanocomposite materials, quantitatively trustworthy results have high importance.

CHAPTER 7 : Appendix

7.1. Entropy and Potential Energy Derivation

To derive the expressions for the entropic and enthalpic components of the free energy, we begin by applying the mean field approximation to our canonical partition function, resulting in

$$\mathcal{Z} = z_1 \exp\left(-\mathcal{H}^*\right) \tag{7.1}$$

where $\mathcal{H}^*$ is the mean field Hamiltonian and the z_1 term contains a factor of $T^{3n_{sites}/2}$ where $n_{sites} = n_D N + n_{GA} n_P + n_{PF}$. We then insert this expression into equation 2.43. The resulting expression is

$$U = \frac{3n_{sites}}{2} - T\left(\frac{\partial \mathcal{H}^*}{\partial T}\right). \tag{7.2}$$

To evaluate the last term in equation 7.2, we assume that $\kappa \propto 1/T$ and $\chi \propto 1/T$. The only T-dependent terms in $\mathcal{H}^*$ are those containing κ and χ. The resulting expression for U in units of $k_B T$ is

$$U = \frac{3n_{sites}}{2} - \frac{\rho_0}{2\kappa}\int d\mathbf{r} w_+^2(\mathbf{r}) - \frac{\rho_0}{\chi}\int d\mathbf{r}\left(w_{AB}^{(+)^2}(\mathbf{r}) + w_{AB}^{(-)^2}(\mathbf{r})\right). \tag{7.3}$$

Let us define U_{ideal} and U_{excess} as follows:

$$U_{ideal} = \frac{3n_{sites}}{2} \tag{7.4}$$

$$U_{excess} = -\frac{\rho_0}{2\kappa}\int d\mathbf{r} w_+^2(\mathbf{r}) - \frac{\rho_0}{\chi}\int d\mathbf{r}\left(w_{AB}^{(+)^2}(\mathbf{r}) + w_{AB}^{(-)^2}(\mathbf{r})\right). \tag{7.5}$$

Note that U_{ideal} is constant across all NP separation distances Δr. We can use the relationship

$$F = -\log \mathcal{Z} = -\log z_1 + \mathcal{H}^* \tag{7.6}$$

in combination with equation 2.44 to find $-TS$. Here, let us define $F_0 = -\log z_1$, which also is constant across all NP separation distances Δr. If we start with $-TS(\Delta r) = F(\Delta r) - U(\Delta r)$ and subtract the equation $-TS(\Delta r = \infty) = F(\Delta r = \infty) - U(\Delta r = \infty)$, we get $-T\Delta S = \Delta F - \Delta U$, or equivalently, $-T\Delta S = \Delta\mathcal{H}^* - \Delta U_{excess}$.

7.2. Nematic Order Parameter Derivation

Assume we have a system with a diblock chain comprised of N beads and $N-1$ harmonic bonds attaching those beads. The probability of observing bond $s \in [1, N-1]$ at position $\mathbf{r}$ with extension $\delta\mathbf{r}$ is given by the product of the propagator (q) to bead s, the inverse propagator ($q^\dagger$) to bead $s+1$, and the normalized bond potential (Φ) as follows:

$$P(s;\mathbf{r},\delta\mathbf{r}) = \frac{1}{Q_d} q\left(s, \mathbf{r} - \frac{1}{2}\delta\mathbf{r}\right) \Phi(\delta\mathbf{r}) q^\dagger\left(N-s, \mathbf{r} + \frac{1}{2}\delta\mathbf{r}\right) \tag{7.7}$$

Here, $\mathbf{r}$ is the position of the bond, taken as the halfway point between the beads it connects. To get equation 7.7 in a more tractable form, we can approximate it with a second order Taylor series expansion as follows:

$$\begin{aligned}
P(s;\mathbf{r},\delta\mathbf{r}) = \frac{\Phi(\delta\mathbf{r})}{Q_d} &\left[q(s,\mathbf{r}) - \frac{1}{2}\delta\mathbf{r}\cdot\nabla q(s,\mathbf{r}) + \frac{1}{8}(\delta\mathbf{r}\cdot\nabla)^2 q(s,\mathbf{r}) + \mathcal{O}(\delta r^3)\right] \\
&\times \left[q^\dagger(N-s,\mathbf{r}) + \frac{1}{2}\delta\mathbf{r}\cdot\nabla q^\dagger(N-s,\mathbf{r}) + \frac{1}{8}(\delta\mathbf{r}\cdot\nabla)^2 q^\dagger(N-s,\mathbf{r}) + \mathcal{O}(\delta r^3)\right] \\
= \frac{\Phi(\delta\mathbf{r})}{Q_d} &\left[q(s,\mathbf{r})q^\dagger(N-s,\mathbf{r}) + \frac{1}{2}\delta\mathbf{r}\cdot\nabla\left(q^\dagger(N-s,\mathbf{r})q(s,\mathbf{r}) - q(s,\mathbf{r})q^\dagger(N-s,\mathbf{r})\right)\right. \\
&\quad - \frac{1}{4}\delta\mathbf{r}\cdot\nabla q(s,\mathbf{r})\delta\mathbf{r}\cdot\nabla q^\dagger(N-s,\mathbf{r}) \\
&\quad \left. + \frac{1}{8}(\delta\mathbf{r}\cdot\nabla)^2\left(q(s,\mathbf{r})q^\dagger(N-s,\mathbf{r}) + q^\dagger(N-s,\mathbf{r})q(s,\mathbf{r})\right)\right] + \mathcal{O}(\delta r^3)
\end{aligned} \tag{7.8}$$

The ijth component of the nematic order tensor is given by

$$S_{ij}(\mathbf{r}) = \int d(\delta\mathbf{r}) \frac{1}{N-1} \sum_{s=1}^{N-1} P(s;\mathbf{r},\delta\mathbf{r}) \left(\frac{\delta r_i \delta r_j}{b^2} - \frac{\delta_{ij}}{3} \frac{|\delta\mathbf{r}|^2}{b^2} \right). \tag{7.9}$$

To derive expressions for the elements of $\mathbf{S}$, we split $P(s;\mathbf{r},\delta\mathbf{r})$ into 4 terms such that

$$P = P_1 + P_2 + P_3 + P_4 \tag{7.10}$$

$$P_1(s;\mathbf{r},\delta\mathbf{r}) = \frac{\Phi(\delta\mathbf{r})}{Q_d} q(s,\mathbf{r}) q^\dagger(N-s,\mathbf{r}) \tag{7.11}$$

$$P_2(s;\mathbf{r},\delta\mathbf{r}) = \frac{1}{2} \frac{\Phi(\delta\mathbf{r})}{Q_d} \delta\mathbf{r} \cdot \nabla \left(q^\dagger(N-s,\mathbf{r}) q(s,\mathbf{r}) - q(s,\mathbf{r}) q^\dagger(N-s,\mathbf{r}) \right) \tag{7.12}$$

$$P_3(s;\mathbf{r},\delta\mathbf{r}) = -\frac{1}{4} \frac{\Phi(\delta\mathbf{r})}{Q_d} \delta\mathbf{r} \cdot \nabla q(s,\mathbf{r}) \delta\mathbf{r} \cdot \nabla q^\dagger(N-s,\mathbf{r}) \tag{7.13}$$

$$P_4(s;\mathbf{r},\delta\mathbf{r}) = \frac{1}{8} \frac{\Phi(\delta\mathbf{r})}{Q_d} (\delta\mathbf{r} \cdot \nabla)^2 \left(q(s,\mathbf{r}) q^\dagger(N-s,\mathbf{r}) + q^\dagger(N-s,\mathbf{r}) q(s,\mathbf{r}) \right) \tag{7.14}$$

Next, we use

$$S_{ij}(\mathbf{r}) = \sum_{k=1}^{4} S_{ij}(\mathbf{r};k) \tag{7.15}$$

where

$$S_{ij}(\mathbf{r};k) = \frac{1}{N-1} \int d(\delta\mathbf{r}) \sum_{s=1}^{N-1} P_k(s;\mathbf{r},\delta\mathbf{r}) \left(\frac{\delta r_i \delta r_j}{b^2} - \frac{\delta_{ij}}{3} \frac{|\delta\mathbf{r}|^2}{b^2} \right). \tag{7.16}$$

For each $k \in [1,4]$, we'll derive the expression for one diagonal element, $S_{xx}(\mathbf{r},k)$, and one off-diagonal element, $S_{xy}(\mathbf{r},k)$, and generalize for all elements. We begin with $k = 1$.

Diagonal elements evaluate to 0 as shown here:

$$\begin{aligned} S_{xx}(\mathbf{r};1) &= \frac{1}{Q_d b^2(N-1)} \sum_{s=1}^{N-1} q(s,\mathbf{r}) q^\dagger(N-s,\mathbf{r}) \int d(\delta\mathbf{r}) \Phi(\delta\mathbf{r}) \left(\delta r_x^2 - \frac{1}{3}(\delta r_x^2 + \delta r_y^2 + \delta r_z^2) \right) \\ &= \frac{1}{Q_d b^2(N-1)} \sum_{s=1}^{N-1} q(s,\mathbf{r}) q^\dagger(N-s,\mathbf{r}) \left(\frac{b^2}{3} - \frac{1}{3}(3\frac{b^2}{3}) \right) \\ &= 0 \end{aligned} \tag{7.17}$$

where the integral is evaluated by making use of

$$\int d(\delta\mathbf{r}) \Phi(\delta\mathbf{r}) \delta r_i \delta r_j = \delta_{ij} \frac{b^2}{3}. \tag{7.18}$$

Off-diagonal elements also evaluate to 0 as shown here:

$$S_{xy}(\mathbf{r};1) = \frac{1}{Q_d b^2(N-1)} \sum_{s=1}^{N-1} q(s,\mathbf{r}) q^\dagger(N-s,\mathbf{r}) \int d(\delta\mathbf{r}) \Phi(\delta\mathbf{r}) \delta r_x \delta r_y = 0 \tag{7.19}$$

We now look at $k = 2$. Diagonal elements evaluate to 0 as shown here:

$$\begin{aligned} S_{xx}(\mathbf{r};2) &= \frac{1}{2Q_d b^2(N-1)} \sum_{s=1}^{N-1} \sum_{k \in \{x,y,z\}} \left(q(s,\mathbf{r}) \nabla_k q^\dagger(N-s,\mathbf{r}) - q^\dagger(N-s,\mathbf{r}) \nabla_k q(s,\mathbf{r}) \right) \\ &\quad \times \int d(\delta\mathbf{r}) \Phi(\delta\mathbf{r}) \delta r_k \left(\delta r_x^2 - \frac{1}{3} \left(\delta r_x^2 + \delta r_y^2 + \delta r_z^2 \right) \right) \\ &= 0 \end{aligned} \tag{7.20}$$

Off-diagonal elements also evaluate to 0 as shown here:

$$S_{ij}(\mathbf{r};2) = \frac{1}{2Q_d b^2(N-1)} \sum_{s=1}^{N-1} \sum_{k\in\{x,y,z\}} \Big(q(s,\mathbf{r})\nabla_k q^\dagger(N-s,\mathbf{r}) - q^\dagger(N-s,\mathbf{r})\nabla_k q(s,\mathbf{r}) \Big) \tag{7.21}$$

$$\times \int d(\delta\mathbf{r})\Phi(\delta\mathbf{r})\delta r_i \delta r_j \delta r_k \tag{7.22}$$

$$= 0 \tag{7.23}$$

In both of these cases, the terms evaluate to zero because $\int d(\delta\mathbf{r})\Phi(\delta\mathbf{r})\delta r_i\delta r_j\delta r_k = 0$. The terms associated with $k = 3$ are the first non-zero ones. Below is the derivation for a diagonal term. The notation has been shortened here to save space.

$$\begin{aligned}
S_{xx}(\mathbf{r};3) &= -\frac{1}{4Q_d b^2(N-1)} \sum_s \sum_k \sum_l \nabla_k q \nabla_l q^\dagger \int d(\delta\mathbf{r})\Phi(\delta\mathbf{r})\delta r_k \delta r_l \left(\delta r_x^2 - \frac{1}{3}\left(\delta r_x^2 + \delta r_y^2 + \delta r_z^2\right)\right) \\
&= -\frac{1}{4Q_d b^2(N-1)} \sum_s \sum_k \nabla_k q \nabla_k q^\dagger \int d(\delta\mathbf{r})\Phi(\delta\mathbf{r})\delta r_k^2 \left(\delta r_x^2 - \frac{1}{3}\left(\delta r_x^2 + \delta r_y^2 + \delta r_z^2\right)\right) \\
&= -\frac{1}{4Q_d b^2(N-1)} \sum_s \begin{bmatrix} \nabla_x q \nabla_x q^\dagger \\ \nabla_y q \nabla_y q^\dagger \\ \nabla_z q \nabla_z q^\dagger \end{bmatrix} \cdot \begin{bmatrix} 3\frac{b^4}{9} - \frac{1}{3}\left(3\frac{b^4}{9} + \frac{b^4}{9} + \frac{b^4}{9}\right) \\ 1\frac{b^4}{9} - \frac{1}{3}\left(\frac{b^4}{9} + 3\frac{b^4}{9} + \frac{b^4}{9}\right) \\ 1\frac{b^4}{9} - \frac{1}{3}\left(\frac{b^4}{9} + \frac{b^4}{9} + 3\frac{b^4}{9}\right) \end{bmatrix} \\
&= -\frac{b^2}{36Q_d(N-1)} \sum_s \begin{bmatrix} \nabla_x q \nabla_x q^\dagger \\ \nabla_y q \nabla_y q^\dagger \\ \nabla_z q \nabla_z q^\dagger \end{bmatrix} \cdot \begin{bmatrix} 3 - \frac{5}{3} \\ 1 - \frac{5}{3} \\ 1 - \frac{5}{3} \end{bmatrix} \\
&= -\frac{b^2}{36Q_d(N-1)} \sum_s \left(2\nabla_x q \nabla_x q^\dagger - \frac{2}{3}(\nabla q)\cdot(\nabla q^\dagger)\right)
\end{aligned} \tag{7.24}$$

The integrals were evaluated using the following relationship:

$$\int d(\delta\mathbf{r})\Phi(\delta\mathbf{r})\delta r_x^2 \delta r_k \delta r_l = \frac{b^4}{9}(3\delta_{xk}\delta_{xl} + \delta_{yk}\delta_{yl} + \delta_{zk}\delta_{zl}) \tag{7.25}$$

And here is the derivation for an off-diagonal term:

$$S_{xy}(\mathbf{r};3) = -\frac{1}{4Q_d b^2(N-1)} \sum_s \sum_k \sum_l \nabla_k q \nabla_l q^\dagger \int d(\delta\mathbf{r})\Phi(\delta\mathbf{r})\delta r_x \delta r_y \delta r_k \delta r_l \tag{7.26}$$

The integral evaluates to

$$\int d(\delta\mathbf{r})\Phi(\delta\mathbf{r})\delta r_x \delta r_y \delta r_k \delta r_l = \frac{b^4}{9}(\delta_{xk}\delta_{yl} + \delta_{xl}\delta_{yk}) \tag{7.27}$$

meaning it is $b^4/9$ in 2 cases: 1) $k = x$ and $l = y$, or 2) $k = y$ and $l = x$, and otherwise is zero. With this knowledge, we can simplify equation 7.26 to

$$S_{xy}(\mathbf{r};3) = -\frac{b^2}{36Q_d(N-1)} \sum_s \left(\nabla_x q \nabla_y q^\dagger + \nabla_y q \nabla_x q^\dagger \right) \tag{7.28}$$

Generalizing equations 7.24 and 7.26 to any element of S, we get

$$S_{ij}(\mathbf{r};3) = -\frac{b^2}{36Q_d(N-1)} \sum_s \left[\nabla_i q \nabla_j q^\dagger + \nabla_j q \nabla_i q^\dagger - \frac{2\delta_{ij}}{3}(\nabla q)\cdot(\nabla q^\dagger) \right] \tag{7.29}$$

We now evaluate expression associated with $k = 4$. This expression has 2 terms which we will refer to as 4a and 4b. The math looks very similar for each, so we will evaluate one term (the one containing $q\nabla^2 q^\dagger$) and apply the same treatment to the other. First, we evaluate

the expression for a diagonal term, $S_{xx}(\mathbf{r};4a)$:

$$\begin{aligned}
S_{xx}(\mathbf{r};4a) &= \frac{1}{8Q_d b^2(N-1)} \sum_s \sum_k \sum_l q\nabla_k\nabla_l q^\dagger \int d(\delta\mathbf{r})\Phi(\delta\mathbf{r})\delta r_k \delta r_l \left(\delta r_x^2 - \frac{1}{3}(\delta r_x^2 + \delta r_y^2 + \delta r_z^2)\right) \\
&= \frac{1}{8Q_d b^2(N-1)} \sum_s \sum_k q\nabla_k^2 q^\dagger \int d(\delta\mathbf{r})\Phi(\delta\mathbf{r})\delta r_k^2 \left(\delta r_x^2 - \frac{1}{3}(\delta r_x^2 + \delta r_y^2 + \delta r_z^2)\right) \\
&= \frac{1}{8Q_d b^2(N-1)} \sum_s \begin{bmatrix} q\nabla_x^2 q^\dagger \\ q\nabla_y^2 q^\dagger \\ q\nabla_z^2 q^\dagger \end{bmatrix} \cdot \begin{bmatrix} 3\frac{b^4}{9} - \frac{1}{3}\left(3\frac{b^4}{9} + \frac{b^4}{9} + \frac{b^4}{9}\right) \\ 1\frac{b^4}{9} - \frac{1}{3}\left(\frac{b^4}{9} + 3\frac{b^4}{9} + \frac{b^4}{9}\right) \\ 1\frac{b^4}{9} - \frac{1}{3}\left(\frac{b^4}{9} + \frac{b^4}{9} + 3\frac{b^4}{9}\right) \end{bmatrix} \\
&= \frac{b^2}{72Q_d(N-1)} \sum_s \begin{bmatrix} q\nabla_x^2 q^\dagger \\ q\nabla_y^2 q^\dagger \\ q\nabla_z^2 q^\dagger \end{bmatrix} \cdot \begin{bmatrix} 3 - \frac{5}{3} \\ 1 - \frac{5}{3} \\ 1 - \frac{5}{3} \end{bmatrix} \\
&= \frac{b^2}{72Q_d(N-1)} \sum_s \left(2q\nabla_x^2 q^\dagger - \frac{2}{3} q(\nabla\cdot\nabla)q^\dagger\right) \\
&= \frac{b^2}{36Q_d(N-1)} \sum_s \left(q\nabla_x^2 q^\dagger - \frac{1}{3} q(\nabla\cdot\nabla)q^\dagger\right)
\end{aligned} \tag{7.30}$$

For an off-diagonal term:

$$\begin{aligned}
S_{xy}(\mathbf{r};4a) &= \frac{1}{8Q_d b^2(N-1)} \sum_s \sum_k \sum_l q\nabla_k\nabla_l q^\dagger \int d(\delta\mathbf{r})\Phi(\delta\mathbf{r})\delta r_x \delta r_y \delta r_k \delta r_l \\
&= \frac{b^2}{72Q_d(N-1)} \sum_s \left(q\nabla_x\nabla_y q^\dagger + q\nabla_y\nabla_x q^\dagger\right) \\
&= \frac{b^2}{36Q_d(N-1)} \sum_s q\nabla_x\nabla_y q^\dagger
\end{aligned} \tag{7.31}$$

Generalizing equations 7.30 and 7.31 to any element of $\mathbf{S}$:

$$S_{ij}(\mathbf{r};4a) = \frac{b^2}{36Q_d(N-1)} \sum_s \left(q\nabla_i\nabla_j q^\dagger - \frac{\delta_{ij}}{3} q(\nabla\cdot\nabla)q^\dagger\right) \tag{7.32}$$

Applying the same process to term 4b (the term with $q^\dagger \nabla^2 q$) and combining with equation 7.32, we can determine that term 4 is

$$S_{ij}(\mathbf{r};4) = \frac{b^2}{36Q_d(N-1)} \sum_s \left(q\nabla_i\nabla_j q^\dagger + q^\dagger \nabla_i \nabla_j q - \frac{\delta_{ij}}{3}\left[q(\nabla\cdot\nabla)q^\dagger + q^\dagger(\nabla\cdot\nabla)q \right] \right) \tag{7.33}$$

Adding the third and fourth terms (equations 7.29 and 7.33) together, we get:

$$\begin{aligned} S_{ij}(\mathbf{r}) = \frac{b^2}{36Q_d(N-1)} \sum_{s=1}^{N-1} \Bigg(& q\nabla_i\nabla_j q^\dagger + q^\dagger \nabla_i \nabla_j q - \nabla_i q \nabla_j q^\dagger - \nabla_j q \nabla_i q^\dagger \\ & - \frac{\delta_{ij}}{3}\left[q(\nabla\cdot\nabla)q^\dagger + q^\dagger(\nabla\cdot\nabla)q - 2(\nabla q)\cdot(\nabla q^\dagger) \right] \Bigg) \end{aligned} \tag{7.34}$$

where, as a reminder, q is a shorthand for $q(s,\mathbf{r})$ and $q^\dagger$ is a shorthand for $q^\dagger(N-s,\mathbf{r})$.

BIBLIOGRAPHY

[1] P. Akcora, H. Liu, S. K. Kumar, J. Moll, Y. Li, B. C. Benicewicz, L. S. Schadler, D. Acehan, A. Z. Panagiotopoulos, V. Pryamitsyn, V. Ganesan, J. Ilavsky, P. Thiyagarajan, R. H. Colby, and J. F. Douglas. Anisotropic self-assembly of spherical polymer-grafted nanoparticles. *Nat. Mater.*, 8(4):354–9, 2009.

[2] D. J. Audus, K. T. Delaney, H. D. Ceniceros, and G. H. Fredrickson. Comparison of Pseudospectral Algorithms for Field-Theoretic Simulations of Polymers. *Macromolecules*, 46(20):8383–8391, 2013.

[3] A. Bansal, H. Yang, C. Li, B. C. Benicewicz, S. K. Kumar, and L. S. Schadler. Controlling the thermomechanical properties of polymer nanocomposites by tailoring the polymerparticle interface. *Journal of Polymer Science Part B: Polymer Physics*, 44(20):2944–2950, 2006.

[4] F. S. Bates and G. H. Fredrickson. Block Copolymers–Designer Soft Materials. *Physics Today*, 52(2):32, 1999.

[5] L. L. Beecroft and C. K. Ober. Nanocomposite Materials for Optical Applications. *Chemistry of Materials*, 9(6):1302–1317, 1997.

[6] M. R. Bockstaller, Y. Lapetnikov, S. Margel, and E. L. Thomas. Size-Selective Organization of Enthalpic Compatibilized Nanocrystals in Ternary Block Copolymer/Particle Mixtures. *Journal of the American Chemical Society*, 125(18):5276–5277, 2003.

[7] M. R. Bockstaller, R. A. Mickiewicz, and E. L. Thomas. Block copolymer nanocomposites: Perspectives for tailored functional materials. *Adv. Mater.*, 17:1331–1349, 2005.

[8] R. P. Brent. *Algorithms for minimization without derivatives (Prentice-Hall series in automatic computation)*. Prentice-Hall, 1972.

[9] P. M. Chaikin and T. C. Lubensky. *Principles of Condensed Matter Physics*. Cambridge University Press, 1995.

[10] H. Chao, B. A. Hagberg, and R. A. Riggleman. The distribution of homogeneously grafted nanoparticles in polymer thin films and blends. *Soft matter*, 10(40):8083–94, 2014.

[11] H. Chao, J. Koski, and R. A. Riggleman. Solvent vapor annealing in block copolymer nanocomposite films: a dynamic mean field approach. *Soft matter*, (13):239–249, 2017.

[12] X. C. Chen and P. F. Green. Structure of thin film polymer/nanoparticle systems: polystyrene (PS) coated-Au nanoparticle/tetramethyl bisphenol-A polycarbonate mixtures (TMPC). *Soft Matter*, 7(3):1192–1198, 2011.

[13] J. J. Chiu, B. J. Kim, E. J. Kramer, and D. J. Pine. Control of nanoparticle location in block copolymers. *Journal of the American Chemical Society*, 127(14):5036–7, 2005.

[14] Y. I. Derikov, C. Abetz, G. A. Shandryuk, R. V. Talroze, A. A. Ezhov, V. Abetz, Y. V. Kudryavtsev, and M. A. Osipov. Stabilization of Gold Nanospheres and Nanorods in Diblock Copolymers of Styrene and Vinylpyridine. *Polymer Science, Series C*, 60(1):78–85, 2018.

[15] M. Deserno and C. Holm. How to mesh up ewald sums. ii. an accurate error estimate for the particleparticleparticle-mesh algorithm. *The Journal of Chemical Physics*, 109(18):7694–7701, 1998.

[16] R. D. Deshmukh, Y. Liu, and R. J. Composto. Two-dimensional confinement of nanorods in block copolymer domains. *Nano Lett.*, 7:3662–3668, 2007.

[17] H. B. Eitouni and N. P. Balsara. Thermodynamics of Polymer Blends: Datasheet from "Physical Properties of Polymers Handbook" in SpringerMaterials (https://dx.doi.org/10.1007/978-0-387-69002-5_19), 2007.

[18] G. H. Fredrickson. *The Equilibrium Theory of Inhomogeneous Polymers*. Oxford University Press, New York, 2006.

[19] G. H. Fredrickson, V. Ganesan, and F. Drolet. Field-theoretic computer simulation methods for polymers and complex fluids. *Macromolecules*, 35(1):16–39, 2002.

[20] D. Frenkel and B. Smit, editors. *Understanding Molecular Simulation: From Algorithms to Applications*. Academic Press, Inc., Orlando, FL, USA, 1st edition, 1996.

[21] A. L. Frischknecht, M. J. A. Hore, J. Ford, and R. J. Composto. Dispersion of polymer-grafted nanorods in homopolymer films: theory and experiment. *Macromolecules*, 46(7):2856–2869, 2013.

[22] R. Gangopadhyay and A. De. Conducting polymer nanocomposites: A brief overview. *Chemistry of Materials*, 12(3):608–622, 2000.

[23] V. V. Ginzburg. Polymer-Grafted Nanoparticles in Polymer Melts: Modeling Using the Combined SCFT–DFT Approach. *Macromolecules*, 46(24):9798–9805, 2013.

[24] P. F. Green. The structure of chain end-grafted nanoparticle/homopolymer nanocomposites. *Soft Matter*, 7(18):7914, 2011.

[25] N. Grnbech-Jensen and O. Farago. A simple and effective verlet-type algorithm for simulating langevin dynamics. *Molecular Physics*, 111(8):983–991, 2013.

[26] A. Halevi, S. Halivni, M. Oded, A. H. E. Müller, U. Banin, and R. Shenhar. Co-Assembly of A–B Diblock Copolymers with B-type Nanoparticles in Thin Films: Effect of Copolymer Composition and Nanoparticle Shape. *Macromolecules*, 47(9):3022–3032, 2014.

[27] L. M. Hall and K. S. Schweizer. Many body effects on the phase separation and structure of dense polymer-particle melts. *The Journal of chemical physics*, 128(23):234901, jun 2008.

[28] E. Helfand. Theory of inhomogeneous polymers: Fundamentals of the Gaussian random-walk model. *J. Chem. Phys.*, 62:999, 1975.

[29] R. W. Hockney and E. J. W. *Computer Simulation Using Particles*. Routledge, 1989.

[30] T. N. Hoheisel, K. Hur, and U. B. Wiesner. Block Copolymer–Nanoparticle Hybrid Self-Assembly. *Prog. Polym. Sci.*, 2014.

[31] J. B. Hooper and K. S. Schweizer. Contact aggregation, bridging, and steric stabilization in dense polymer-particle mixtures. *Macromolecules*, 38(21):8858–8869, 2005.

[32] J. B. Hooper and K. S. Schweizer. Theory of Phase Separation in Polymer Nanocomposites. *Macromolecules*, 39:5133–5142, 2006.

[33] M. J. A. Hore and R. J. Composto. Using miscible polymer blends to control depletion–attraction forces between Au nanorods in nanocomposite films. *Macromolecules*, 45(15):6078–6086, 2012.

[34] M. J. A. Hore and R. J. Composto. Functional polymer nanocomposites enhanced by nanorods. *Macromolecules*, 47(3):875–887, 2014.

[35] S.-W. Hsu and T. Xu. Tailoring Co-assembly of Nanodiscs and Block Copolymer-Based Supramolecules by Manipulating Interparticle Interactions. *Macromolecules*, 52(7):2833–2842, 2019.

[36] K. Hur, R. G. Hennig, F. A. Escobedo, and U. Wiesner. Mesoscopic structure prediction of nanoparticle assembly and coassembly: theoretical foundation. *J. Chem. Phys.*, 133(19):194108, 2010.

[37] K. Hur, R. G. Hennig, F. a. Escobedo, and U. Wiesner. Predicting chiral nanostructures, lattices and superlattices in complex multicomponent nanoparticle self-assembly. *Nano Lett.*, 12(6):3218–3223, 2012.

[38] A. Jayaraman and K. S. Schweizer. Effective interactions and self-Assembly of hybrid polymer grafted nanoparticles in a homopolymer matrix. *Macromolecules*, 42(21):8423–8434, 2009.

[39] H. Kang, F. b. ç. A. Detcheverry, A. N. Mangham, M. P. Stoykovich, K. C. Daoulas, R. J. Hamers, M. Müller, J. J. de Pablo, and P. F. Nealey. Hierarchical Assembly of Nanoparticle Superstructures from Block Copolymer-Nanoparticle Composites. *Phys. Rev. Lett.*, 100(14):148303, 2008.

[40] J. Kao, K. Thorkelsson, P. Bai, B. J. Rancatore, and T. Xu. Toward functional nanocomposites: Taking the best of nanoparticles, polymers, and small molecules. *Chemical Society Reviews*, 42(7):2654–2678, 2013.

[41] J. Kao and T. Xu. Nanoparticle assemblies in supramolecular nanocomposite thin films: Concentration dependence. *Journal of the American Chemical Society*, 137(19):6356–6365, 2015.

[42] B. J. Kim, J. Bang, C. J. Hawker, and E. J. Kramer. Effect of Areal Chain Density on the Location of Polymer-Modified Gold Nanoparticles in a Block Copolymer Template. *Macromolecules*, 39(12):4108–4114, 2006.

[43] B. J. Kim, G. H. Fredrickson, and E. J. Kramer. Effect of Polymer Ligand Molecular Weight on Polymer-Coated Nanoparticle Location in Block Copolymers. *Macromolecules*, 41(2):436–447, 2008.

[44] J. Kim and P. F. Green. Phase behavior of thin film brush-coated nanoparticles/homopolymer mixtures. *Macromolecules*, 43(3):1524–1529, 2010.

[45] Y. Kim, H. Chen, and A. Alexander-Katz. Free energy landscape and localization of nanoparticles at block copolymer model defects. *Soft Matter*, pages 3284–3291, 2014.

[46] J. R. Klauder. Coherent-state Langevin equations for canonical quantum systems with applications to the quantized Hall effect. *Phys. Rev. A*, 29(4):2036, 1984.

[47] J. Koski, H. Chao, and R. A. Riggleman. Field theoretic simulations of polymer nanocomposites. *The Journal of chemical physics*, 139(24):244911, 2013.

[48] J. Koski, H. Chao, and R. A. Riggleman. Predicting the structure and interfacial activity of diblock brush, mixed brush, and Janus-grafted nanoparticles. *Chemical Communications (Cambridge, United Kingdom)*, 51(25):5440–5443, 2015.

[49] J. Koski, B. Hagberg, and R. A. Riggleman. Attraction of Nanoparticles to Tilt Grain Boundaries in Block Copolymers. *Macromolecular Chemistry and Physics*, 217(3):509–518, 2016.

[50] J. P. Koski, R. C. Ferrier, N. M. Krook, H. Chao, R. J. Composto, A. L. Frischknecht, and R. A. Riggleman. Comparison of Field-Theoretic Approaches in Predicting Polymer Nanocomposite Phase Behavior. *Macromolecules*, 50(21):8797–8809, 2017.

[51] N. M. Krook, J. Ford, M. Maréchal, P. Rannou, J. S. Meth, C. B. Murray, and R. J. Composto. Alignment of Nanoplates in Lamellar Diblock Copolymer Domains and the Effect of Particle Volume Fraction on Phase Behavior. *ACS Macro Letters*, pages 1400–1407, 2018.

[52] S. K. Kumar, V. Ganesan, and R. A. Riggleman. Perspective: Outstanding theoretical questions in polymer-nanoparticle hybrids. *Journal of Chemical Physics*, 147(2), 2017.

[53] S. K. Kumar, N. Jouault, B. Benicewicz, and T. Neely. Nanocomposites with Polymer Grafted Nanoparticles. *Macromolecules*, 46(9):3199–3214, may 2013.

[54] Q. Lan, L. F. Francis, and F. S. Bates. Silica nanoparticle dispersions in homopolymer versus block copolymer. *J. Polym. Sci. Part B Polym. Phys.*, 45(16):2284–2299, 2007.

[55] E. M. Lennon, G. O. Mohler, H. D. Ceniceros, C. J. García-Cervera, and G. H. Fredrickson. Numerical solutions of the complex Langevin equations in polymer field theory. *Multiscale Modeling and Simulation*, 6:1347, 2008.

[56] W. Li, P. Zhang, M. Dai, J. He, T. Babu, Y.-l. Xu, R. Deng, R. Liang, M.-h. Lu, Z. Nie, and J. Zhu. Ordering of Gold Nanorods in Confined Spaces by Directed Assembly. *Macromolecules*, 46:2241, 2013.

[57] Y. Lin, A. Böker, J. He, K. Sill, H. Xiang, C. Abetz, X. Li, J. Wang, T. Emrick, S. Long, Q. Wang, A. Balazs, and T. P. Russell. Self-directed self-assembly of nanoparticle/copolymer mixtures. *Nature*, 434(7029):55–9, 2005.

[58] J. Listak and M. R. Bockstaller. Stabilization of grain boundary morphologies in lamellar block copolymer/nanoparticle blends. *Macromolecules*, 39(17):5820–5825, 2006.

[59] Y. Liu, M. H. Rafailovich, J. Sokolov, S. A. Schwarz, X. Zhong, A. Eisenberg, E. J. Kramer, B. B. Sauer, and S. Satija. Wetting behavior of homopolymer films on chemically similar block copolymer surfaces. *Physical Review Letters*, 73(3):440–443, 1994.

[60] Z. Liu, H. Huang, and T. He. Large-area 2D gold nanorod arrays assembled on block copolymer templates. *Small*, 9:505–510, 2013.

[61] M. W. Matsen and F. S. Bates. Unifying weak- and strong-segregation block copolymer theories. *Macromolecules*, 29(4):1091–1098, 1996.

[62] M. W. Matsen and J. M. Gardiner. Autophobic dewetting of homopolymer on a brush and entropic attraction between opposing brushes in a homopolymer matrix. *Journal of Chemical Physics*, 115(6):2794–2804, 2001.

[63] M. W. Matsen and R. B. Thompson. Particle Distributions in a Block Copolymer Nanocomposite. *Macromolecules*, 41(5):1853–1860, 2008.

[64] J. F. Moll, P. Akcora, A. Rungta, S. Gong, R. H. Colby, B. C. Benicewicz, and S. K. Kumar. Mechanical reinforcement in polymer melts filled with polymer grafted nanoparticles. *Macromolecules*, 44(18):7473–7477, 2011.

[65] G. Parisi. On complex probabilities. *Phys. Lett. B*, 131(4-6):393–395, 1983.

[66] E. Ploshnik, A. Salant, U. Banin, and R. Shenhar. Co-assembly of block copolymers and nanorods in ultrathin films: effects of copolymer size and nanorod filling fraction. *Physical chemistry chemical physics : PCCP*, 12(38):11885–11893, 2010.

[67] E. Ploshnik, A. Salant, U. Banin, and R. Shenhar. Hierarchical Surface Patterns of Nanorods Obtained by Co-Assembly with Block Copolymers in Ultrathin Films. *Advanced Materials*, 22(25):2774–2779, 2010.

[68] I. Prasad, Y. Seo, L. M. Hall, and G. M. Grason. Intradomain Textures in Block Copolymers: Multizone Alignment and Biaxiality. *Physical Review Letters*, 118(24):1–6, 2017.

[69] B. Rasin, H. Chao, G. Jiang, D. Wang, R. A. Riggleman, and R. J. Composto. Dispersion and alignment of nanorods in cylindrical block copolymer thin films. *Soft Matter*, 12(7):2177–2185, 2016.

[70] G. Reiter and R. Khanna. Negative Excess Interfacial Entropy between Free and End-Grafted Chemically Identical Polymers. *Physical Review Letters*, 85(26):5599–5602, 2000.

[71] R. A. Riggleman and G. H. Fredrickson. Field-theoretic simulations in the Gibbs ensemble. *Journal of Chemical Physics*, 132(2):024104/1–024104/12, jan 2010.

[72] R. A. Riggleman, R. Kumar, and G. H. Fredrickson. Investigation of the interfacial tension of complex coacervates using field-theoretic simulations. *Journal of Chemical Physics*, 136:24903, 2012.

[73] H. J. Ryu, D. B. Fortner, S. Lee, R. Ferebee, M. De Graef, K. Misichronis, A. Avgeropoulos, and M. R. Bockstaller. Role of grain boundary defects during grain coarsening of lamellar block copolymers. *Macromolecules*, 46(1):204–215, 2013.

[74] H. J. Ryu, J. Sun, A. Avgeropoulos, and M. R. Bockstaller. Retardation of grain growth and grain boundary pinning in athermal block copolymer blend systems. *Macromolecules*, 47(4):1419–1427, 2014.

[75] V. Sankaran, R. E. Cohen, C. C. Cummins, R. R. Schrock, and R. J. Silbey. Small PbS Clusters Prepared via ROMP Block Copolymer Technology. *Journal of the American Chemical Society*, 112(19):6858–6859, 1990.

[76] B. Sarkar and P. Alexandridis. Block copolymer-nanoparticle composites: Structure, functional properties, and processing. *Progress in Polymer Science*, 40(1):33–62, 2015.

[77] K. S. Schweizer and J. G. Curro. *Integral Equation Theories of the Structure, Thermodynamics, and Phase Transitions of Polymer Fluids*, pages 1–142. John Wiley & Sons, Ltd, 1997.

[78] A.-C. Shi and J. Noolandi. Theory of inhomogeneous weakly charged polyelectrolytes. *Macromolecular Theory and Simulations*, 8(3):214–229, 1999.

[79] S. W. Sides, B. J. Kim, E. J. Kramer, and G. H. Fredrickson. Hybrid particle-field simulations of polymer nanocomposites. *Physical Review Letters*, 96(25):250601, 2006.

[80] M. P. Stoykovich, H. Kang, K. C. Daoulas, G. Liu, C. Liu, J. J. D. Pablo, M. Müller, and P. F. Nealey. Directed Self-Assembly of Block Copolymers for Nanolithography : Essential Integrated Circuit Geometries. *Acsnano*, 1(3):168–175, 2007.

[81] M. P. Stoykovich, M. Müller, S. O. Kim, H. H. Solak, W. Erik, J. J. D. Pablo, and P. F. Nealey. Directed Assembly of Block Copolymer Blends into Nonregular Device-Oriented Structures. *Science*, 308(5727):1442–1446, 2012.

[82] R. B. Thompson, V. V. Ginzburg, M. W. Matsen, and A. C. Balazs. Predicting the mesophases of copolymer-nanoparticle composites. *Science*, 292(5526):2469–2472, 2001.

[83] R. B. Thompson, V. V. Ginzburg, M. W. Matsen, and A. C. Balazs. Block copolymer-directed assembly of nanoparticles: Forming mesoscopically ordered hybrid materials. *Macromolecules*, 35(3):1060–1071, 2002.

[84] K. Thorkelsson, N. Bronstein, and T. Xu. Nanorod-Based Supramolecular Nanocomposites: Effects of Nanorod Length. *Macromolecules*, 49(17):6669–6677, 2016.

[85] K. Thorkelsson, A. J. Mastroianni, P. Ercius, and T. Xu. Direct nanorod assembly using block copolymer-based supramolecules. *Nano letters*, 12(1):498–504, 2012.

[86] K. Thorkelsson, J. H. Nelson, A. P. Alivisatos, and T. Xu. End-to-end alignment of nanorods in thin films. *Nano letters*, 13(10):4908–13, 2013.

[87] D. M. Trombly and V. Ganesan. Curvature effects upon interactions of polymer-grafted nanoparticles in chemically identical polymer matrices. *J. Chem. Phys.*, 133(15):1–7, 2010.

[88] M. C. Villet and G. H. Fredrickson. Numerical coarse-graining of fluid field theories. *J. Chem. Phys.*, 132(3):1–8, 2010.

[89] S. C. Warren, F. J. Disalvo, and U. Wiesner. Nanoparticle-tuned assembly and disassembly of mesostructured silica hybrids. *Nature Materials*, 6(2):156–161, 2007.

[90] R. Yamamoto. Novel Thermally Conductive Sheet Applying Orientation Control of Graphite Particles. 13(6):462–468, 2010.

[91] L. Yao, Y. Lin, and J. J. Watkins. Ultrahigh loading of nanoparticles into ordered block copolymer composites. *Macromolecules*, 47(5):1844–1849, 2014.

[92] J. Yin, X. Yao, J.-Y. Liou, W. Sun, Y.-S. Sun, and Y. Wang. Membranes with Highly Ordered Straight Nanopores by Selective Swelling of Fast Perpendicularly Aligned Block Copolymers. *ACS Nano*, 7(11):9961–9974, oct 2013.

[93] X. Zhang, F. K. Lee, and O. K. C. Tsui. Wettability of end-grafted polymer brush by chemically identical polymer films. *Macromolecules*, 41(21):8148–8151, 2008.

[94] Y. Zhao, K. Thorkelsson, A. J. Mastroianni, T. Schilling, J. M. Luther, B. J. Rancatore, K. Matsunaga, H. Jinnai, Y. Wu, D. Poulsen, J. M. J. Fréchet, A. Paul Alivisatos, and T. Xu. Small-molecule-directed nanoparticle assembly towards stimuli-responsive nanocomposites. *Nature Materials*, 8:979, 2009.

[95] Y. Zhou and K. S. Schweizer. Local structure, thermodynamics, and phase behavior of asymmetric particle mixtures: Comparison between integral equation theories and simulation. *Journal of Chemical Physics*, 150(21), 2019.